OPEN JOURNAL OF

# NANO

ISSN:2147-0081

Volume:6, Issue: 2, Year: 2021

A JOURNAL ABOUT NANOSCIENCE

Volume 6 / Issue 2

# Open Journal of Nano

Volume 6 / Issue 2

# Open Journal of Nano

OPEN JOURNAL OF NANO

# Contents
## Volume: 6, Issue: 2, Year: 2021

OPEN JOURNAL OF NANO

# İçindekiler
## Cilt: 6, Sayı: 2, Yıl: 2021

**Open Journal of Nano**
(2021) 6–2

# Molecular Structure and Docking Analysis of the Integrin Inhibitor Cyclo (Arg-Gly-Asp-D-Phe-Val) Peptide

Sefa CELİK[1], Aliye Demet DEMİRAG[2,3], Hira CIVELEK[4], Aysen E. OZEL[1], Sevim AKYUZ[5]

[1]Istanbul University, Faculty of Science, Department of Physics, Vezneciler, Istanbul, 34134, Istanbul
[2] Yeditepe University, Vocational School, Internet and Network Technologies Department, 34755, Istanbul
[3]Istanbul University, Institute of Graduate Studies in Sciences, 34452, Istanbul
[4] Yeditepe University, Vocational School, Mechatronic Department, 34755, Istanbul
[5]Istanbul Kultur University, Faculty of Science and Letters, Department of Physics, 34156, Istanbul
Corresponding author, e-mail: demet.demirag@yeditepe.edu.tr

Submission Date: 08.10.2021 Acceptation Date: 20.11.2021

**Abstract** - All possible conformations of Cyclo (Arg-Gly-Asp-D-Phe-Val) ($C_{26}H_{38}N_8O_7$) with antitumor activity were determined and the most stable conformer elucidated by MMFF method using the Spartan06 program. The differences in energy between the conformers were determined, and the low energy conformers, which are required for determination of the biological activity, were characterized. Since as an anticancer candidate, the investigated molecule is expected to be an integrin inhibitor, a molecular docking study was conducted with $\alpha_v\beta_3$ integrin to determine the mechanism of interaction. As a result of docking simulations, the binding affinity ( $\Delta G$ = -10.5 kcal/mol) and the interactions between the investigated peptide and target integrin were determined.

**Keywords:** Antitumor activity, Spartan06 program, Integrin inhibitor, Docking simulation

## 1. Introduction

Integrins are transmembrane receptors that connect the actin cytoskeleton to the extracellular matrix (ECM). Integrins are multifunctional heterodimers that regulate cell-cell and cell-matrix interactions via signaling and are involved in a number of critical functions, including cell cycle and proliferation control, in part through collaboration with growth factor receptors [1]. This connection is dynamically rearranged as a result of mechanical, chemokine, and growth factor signals. The $\alpha_v\beta_3$ integrin functions as a receptor for vitronectin [2], a cell cell-adhesive protein like fibronectin. The domain 10 of module III ($III_{10}$) of fibronectin comprises the Arginine-Glycine-Asparagine RGD pattern that $\alpha_V\beta_3$ recognizes. For this reason Arg-Gly-Asp (RGD) containing ligands are important for the interactions with integrins. Integrins are heterodimeric transmembrane receptors and mediate cell adhesion. Many cell types' growth and survival have been shown to be dependent on integrin-mediated adherence to extracellular matrix (ECM) protein 1 in recent years [3]. Cell-matrix interactions mediated by integrins control a wide range of biological processes [4]. Cell adhesion, migration, invasion, proliferation, and survival/anoikis are all regulated by integrins' interactions with their substrates, which are also related to tumor growth and metastatic growth [5]. The $\alpha_v\beta_3$ integrin expression in several tumor tissues has strongly suggested that this receptor may have a role in tumor growth, especially in invasive cancers that preferentially metastasize to bone, such as breast and prostate carcinomas [6]. Integrins are being recognized as significant players in tumor biology and may be valuable targets for tumor therapy as more is discovered about the impact of a tumor cell's microenvironment on survival and invasive potential [7]. Recent research has found that $\alpha_v\beta_3$ expression enhances breast cancer spontaneous bone metastasis (Takayama et al., 2005; Sloan et al., 2006), and the functional status of integrin αvβ3 is crucial in many aspects of this process [8].

Following prior research tying its expression to the window of implantation and its absence to infertility problems such as luteal phase insufficiency, endometriosis, hydrosalpinx, and unexplained infertility, the $\alpha_v\beta_3$ integrin has sparked renewed attention [9]. The most common cause of mortality from gynecological illness is ovarian cancer [10]. Women who have ovarian cancer that is solely localized at the time of diagnosis have a good cure rate [11]. However, only around one-fifth of ovarian cancers are identified at this stage, with the majority of cases being discovered after cancer has spread to other parts of the body. Many cancer types, including ovarian cancer cell lines and original tissues from ovarian cancer patients, express $\alpha_v\beta_3$ integrin [12]. There has been a link found between $\alpha_v\beta_3$ integrin expression and ovarian tumor development. The vast majority of tumor vasculature in ovarian carcinomas express this receptor, regardless of v3 expression in the initial tumor [13]. Prostate cancer development has been connected to $\alpha_v\beta_3$ integrin, which has implications for angiogenesis, survival, and invasion. According to the in vitro studies [13,14], integrins helped prostate cancer cells adhere together, migrate through a variety of ECM substrates, and cross the endothelium barrier. The $\alpha_v\beta_3$ integrin receptor, which binds a variety of ligands via an RGD sequence, is prevalent in normal vasculature but is over expressed in tumor vasculature, making it a possible antiangiogenic drug target [15]. The $\alpha_v\beta_3$ integrin expression and activation have also been associated to breast tumors that are more metastatic and aggressive [16]. When $\alpha_v\beta_3$ activity is suppressed by mAb and cyclic RGD peptides, endothelial mortality, angiogenesis suppression, and enhanced endothelial monolayer permeability have all been observed. Inhibiting $\alpha_v\beta_3$ activity has been associated to decreased tumor development in breast cancer xenografts and melanoma xenografts [17].

In this research, the most stable conformation of the Cyclo (Arg-Gly-Asp-D-Phe-Val) peptide was firstly determined. Afterwards, by molecular docking simulations, the binding affinity and the interaction modes of the most stable conformer with $\alpha_v\beta_3$ integrin were revealed.

## 2. Methods and Calculations

Conformational analysis was performed by using The Spartan06 software [18] and the MMFF technique [19]. To determine the probable binding sites on the surface of the receptor, The CAVER software [20] was used. Molecular docking investigations were performed using AutoDock-Vina software on the identified active sites [21].

## 3. Results and Discussions

### 3.1. Structure

As a result of conformational analysis five lowest energy conformers of Cyclo (Arg-Gly-Asp-D-Phe-Val) were determined. The relative energies of these most stable conformers are given in Table 1 and their molecular structures are shown in Figure 1.

**Table 1.** The energies of the most stable five conformations of Cyclo (Arg-Gly-Asp-D-Phe-Val) peptide.

| Conformers | Total energy (kj/mol) | Relative energy (kj/mol) |
|---|---|---|
| ( I ) | -816.4 | 0 |
| ( II ) | -814.2 | 2.2 |
| ( III ) | -812.61 | 3.79 |
| ( IV ) | -812.53 | 3.87 |
| ( V ) | -811.45 | 4.95 |

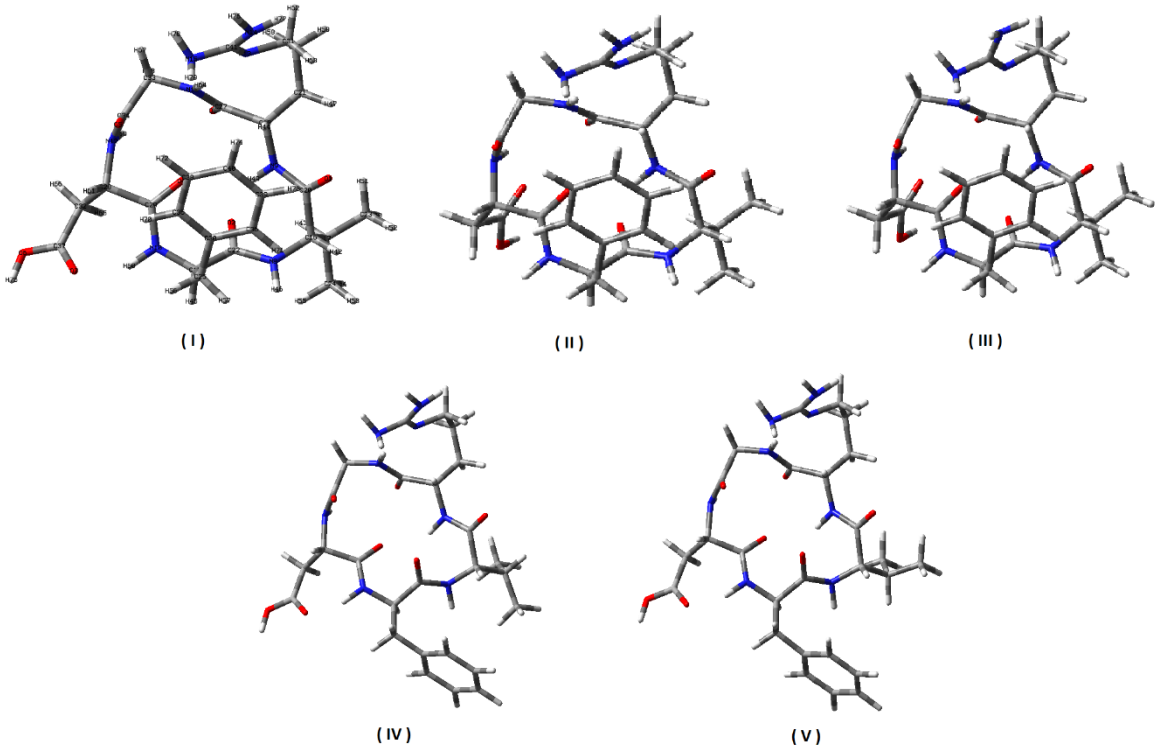


**Figure 1.** The molecular structures of the obtained five lowest energy conformers of Cyclo (Arg-Gly-Asp-D-Phe-Val) by conformational analysis.

### 3.2. Molecular Docking

Molecular docking simulations in target protein $\alpha_v\beta_3$ integrin were calculated to evaluate the anti-proliferation effect of the Cyclo (Arg-Gly-Asp-D-Phe-Val) for the anticancer activity. After preparing the $\alpha_v\beta_3$ integrin (PDB ID: 1JV2) for molecular docking [22], docking simulations of Cyclo (Arg-Gly-Asp-D-Phe-Val) to the $\alpha_v\beta_3$ integrin for the most active site were performed with a binding affinity of -10.5 kcal/mol. The 3D docked view of Cyclo (Arg-Gly-Asp-D-Phe-Val) at the most active region of $\alpha_v\beta_3$ integrin is shown in Figure 2. The Cyclo (Arg-Gly-Asp-D-Phe-Val) - $\alpha_v\beta_3$ integrin complex interaction diagrams are also shown. The revealed interactions between Cyclo (Arg-Gly-Asp-D-Phe-Val) ligand and the target protein $\alpha_v\beta_3$ integrin were as follows:

Between Cyclo (Arg-Gly-Asp-D-Phe-Val) and the amino acid residues of Val23, two hydrogen bonds with 2.41, 3.1Å length, and a unfavorable donor-donor interaction with 2.3Å length; Val98, hydrogen bonds with 1.97 and 2.49 Å length; Arg99, 1.63 and 2.49 Å long unfavorable donor-donor interaction and 1.92 Å long hydrogen bond; Ile161, 3.53 Å long carbon hydrogen bond; Val226, 2.26 Å long hydrogen bond; Ala343, 5.23 Å long Pi-alkyl interaction; Ile344, 2.67 Å long hydrogen bond; Pro346, 1.93 Å long hydrogen bond; Met408, 2.48 Å long hydrogen bond; Gly410, 2.76 Å long hydrogen bond are defined.

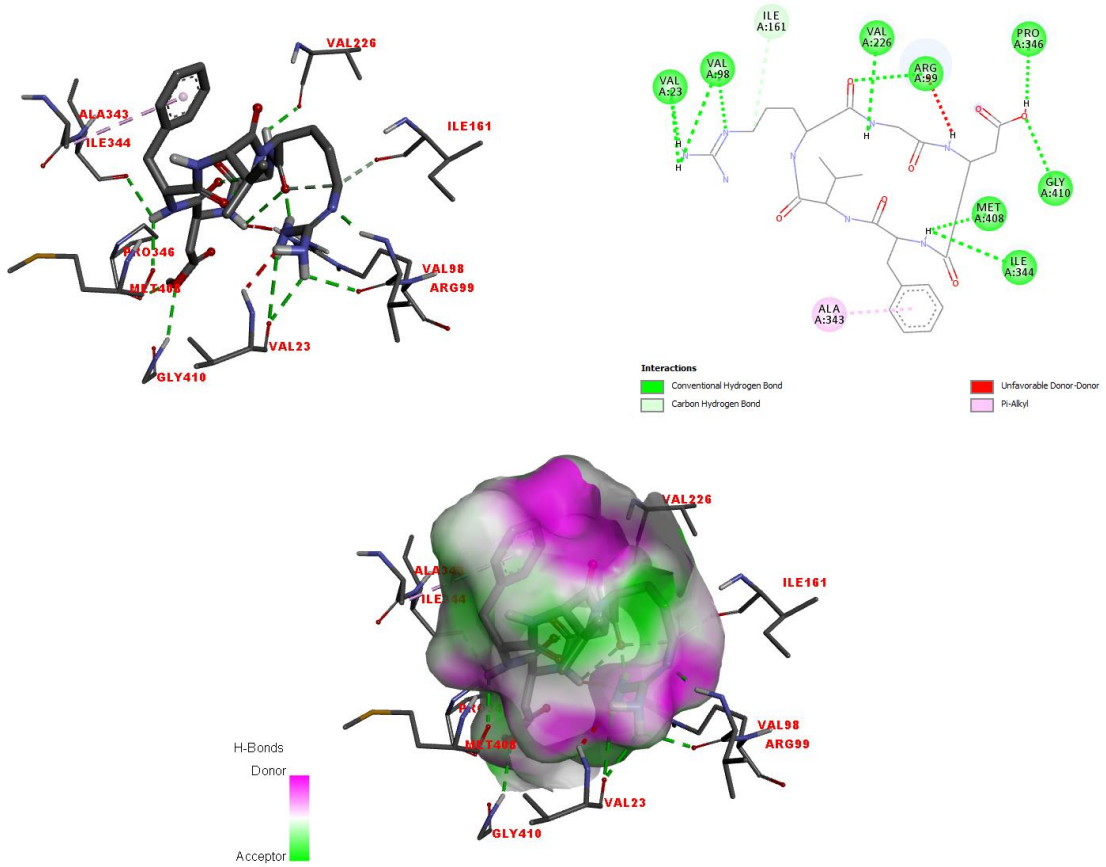


**Figure 2.** The 3D docked views of the most stable conformer of Cyclo (Arg-Gly-Asp-D-Phe-Val) in active site of $\alpha_v\beta_3$ integrin (-10.5 kcal/mol).

## 4. Conclusions

The most stable conformer of cyclic pentapeptide, Cyclo(Arg-Gly-Asp-D-Phe-Val), was determined due to the importance of the function-activity relationship for the bioactive molecules. The interaction of the title molecule with $\alpha_v\beta_3$ integrin was investigated by docking simulations, by using the most stable conformer of the Cyclo(Arg-Gly-Asp-D-Phe-Val), to assess its biological activity and to examine the inhibitory effect on integrin. The binding affinity of cyclo (Arg-Gly-Asp-D-Phe-Val) to $\alpha_v\beta_3$ integrin was found to be -10.5 kcal/mol. According to molecular docking predictions, Cyclo (Arg-Gly-Asp-D-Phe-Val) found to have a good inhibitory effect on $\alpha_v\beta_3$ integrin and may exhibit significant anti-tumor properties.

**Peer-review:** Externally peer - reviewed.

**Conflict of Interest:** No conflict of interest was declared by the authors.

**Financial Disclosure:** The authors declared that this study has received no financial support (If there is financial support, please specify the grant organization and support number).

## References

1. Manninen, A. (2015). Epithelial polarity–generating and integrating signals from the ECM with integrins. Experimental cell research, 334(2), 337-349.
2. Guan, X. (2015). Cancer metastases: challenges and opportunities. Acta pharmaceutica sinica B, 5(5), 402-418.

3. Kantola, A. (2010). Latent TGF-β binding proteins-3 and-4: transcriptional control and extracellular matrix targeting.
4. Rege, T. A., & Hagood, J. S. (2006). Thy-1 as a regulator of cell-cell and cell-matrix interactions in axon regeneration, apoptosis, adhesion, migration, cancer, and fibrosis. The FASEB journal, 20(8), 1045-1054.
5. Sloan, E. K., Pouliot, N., Stanley, K. L., Chia, J., Moseley, J. M., Hards, D. K., & Anderson, R. L. (2006). Tumor-specific expression of αvβ3 integrin promotes spontaneous metastasis of breast cancer to bone. Breast Cancer Research, 8(2), 1-14.
6. Danhier, F., Le Breton, A., & Préat, V. (2012). RGD-based strategies to target alpha (v) beta (3) integrin in cancer therapy and diagnosis. Molecular pharmaceutics, 9(11), 2961-2973.
7. Hamidi, H., & Ivaska, J. (2018). Every step of the way: integrins in cancer progression and metastasis. Nature Reviews Cancer, 18(9), 533-548.
8. Schneider, J. G., Amend, S. R., & Weilbaecher, K. N. (2011). Integrins and bone metastasis: integrating tumor cell and stromal cell interactions. Bone, 48(1), 54-65.
9. Zhang, C., Long, L., & Shi, C. (2018). Mitochondria-targeting IR-780 dye and its derivatives: synthesis, mechanisms of action, and theranostic applications. Advanced Therapeutics, 1(7), 1800069.
10. Senthil, K., Aranganathan, S., & Nalini, N. (2004). Evidence of oxidative stress in the circulation of ovarian cancer patients. Clinica chimica acta, 339(1-2), 27-32.
11. Bolton, K. L., Chenevix-Trench, G., Goh, C., Sadetzki, S., Ramus, S. J., Karlan, B. Y., ... & Pharoah, P. D. (2012). Association between BRCA1 and BRCA2 mutations and survival in women with invasive epithelial ovarian cancer. Jama, 307(4), 382-389.
12. Onda, T., Yoshikawa, H., Yasugi, T., Mishima, M., Nakagawa, S., Yamada, M., ... & Taketani, Y. (1998). Patients with ovarian carcinoma upstaged to stage III after systematic lymphadenctomy have similar survival to Stage I/II patients and superior survival to other Stage III patients. Cancer: Interdisciplinary International Journal of the American Cancer Society, 83(8), 1555-1560.
13. Mattern, J., Koomägi, R., & Volm, M. (1996). Association of vascular endothelial growth factor expression with intratumoral microvessel density and tumour cell proliferation in human epidermoid lung carcinoma. British journal of cancer, 73(7), 931-934.
14. Ganguly, K. K., Pal, S., Moulik, S., & Chatterjee, A. (2013). Integrins and metastasis. Cell adhesion & migration, 7(3), 251-261.
15. Ruoslahti, E. (2000, December). Targeting tumor vasculature with homing peptides from phage display. In Seminars in cancer biology (Vol. 10, No. 6, pp. 435-442). Academic Press.
16. Taherian, A., Li, X., Liu, Y., & Haas, T. A. (2011). Differences in integrin expression and signaling within human breast cancer cells. BMC cancer, 11(1), 1-15.
17. Burke, P. A., DeNardo, S. J., Miers, L. A., Lamborn, K. R., Matzku, S., & DeNardo, G. L. (2002). Cilengitide targeting of αvβ3 integrin receptor synergizes with radioimmunotherapy to increase efficacy and apoptosis in breast cancer xenografts. Cancer research, 62(15), 4263-4272.
18. Shao, Y., Molnar, L. F., Jung, Y., Kussmann, J., Ochsenfeld, C., Brown, S. T., ... & DiStasio Jr, R. A. (2006). Advances in methods and algorithms in a modern quantum chemistry program package. Physical Chemistry Chemical Physics,8(27), 3172-3191.
19. Halgren, T. A. (1996). Merck molecular force field. I. Basis, form, scope, parameterization, and performance of MMFF94. Journal of computational chemistry, 17(5-6), 490-519.

20. Jurcik, A.; Bednar, D.; Byska, J.; Marques, S.M.; Furmanova, K.; Daniel, L.;... Pavelka, A. CAVER Analyst 2.0: analysis and visualization of channels and tunnels in protein structures and molecular dynamics trajectories. *Bioinformatics* **2018**, 34, 3586-3588.
21. Trott, O.; Olson, A.J. AutoDock Vina: Improving the speed and accuracy of docking with a new scoring function, efficient optimization, and multithreading.J. Comput. Chem. 2010,31, 455-461.
22. Xiong, J. P., Stehle, T., Diefenbach, B., Zhang, R., Dunker, R., Scott, D. L., ... & Arnaout, M. A. (2001). Crystal structure of the extracellular segment of integrin $\alpha_V\beta_3$. Science, 294(5541), 339-345.

**Open Journal of Nano**
(2021) 6–2

# Decreasing Defects in Plastic Injection Molding and Vibration Welding Processes Through Statistical Process Control

[1]Meryem Uluskan

[1]Eskişehir Osmangazi University, Department of Industrial Engineering, Eskisehir, Turkey.
Corresponding author, e-mail: muluskan@ogu.edu.tr

Submission Date: 05.11.2021 Acceptation Date: 09.12.2021

**Abstract -** The goal of this study is to decrease a particular defect seen on condenser dryer water tanks, which are manufactured through plastic injection molding and vibration welding. Water leakage problem encountered on these tanks were aimed to be minimized through statistical process control techniques. Initially, the water leakage problem and its criticality was determined by presenting the cost of this problem. After determination of the problem, manufacturing workflow was provided. Next, cause-and-effect diagram presenting the potential causes of water tank leakage was created and the root causes were discussed in detail. Then, control charts were created to examine the process stability. In addition, initial process capability analysis was conducted through which poor capability was revealed. It was determined that both injection molding and vibration welding processes were among the root causes of water leakage problem. Therefore, improvement efforts made included mold maintenance and cleaning, and usage of custom fixtures on the welding machine. After improvements took place, final control charts were created and process capability analyses were re-conducted. Results revealed the fact that the improved molding process was in control and the process capability was enhanced dramatically. In addition, the significance of the improvements made were verified through hypothesis testing. The improvements were standardized for sustainability. Finally, as an additional remedial action, a new automated leakage testing system was designed and utilized as a replacement for the previous manual system. This action also decreased the amount of faulty water tanks that are shipped to the customer.

**Keywords:** Household appliances, Quality improvement, Plastic injection molding, Statistical process control, Vibration welding

# İstatistiksel Süreç Kontrolü ile Plastik Enjeksiyon ve Titreşim Kaynak Süreçlerinde Hataların Azaltılması

**Öz -** Bu çalışmanın amacı, plastik enjeksiyon kalıplama ve vibrasyon kaynağı ile imal edilen kondenser kurutucu su tanklarında görülen belirli bir kusuru azaltmaktır. Bu tanklarda karşılaşılan su sızıntısı sorununun istatistiksel süreç kontrol teknikleri ile en aza indirilmesi hedeflenmiştir. Öncelikle bu problemin maliyeti ortaya konularak su kaçağı problemi ve önemi belirlenmiştir. Problem tespit edildikten sonra imalat iş akışı verilmiştir. Ardından, su deposu sızıntısının olası nedenlerini gösteren neden-sonuç diyagramı oluşturulmuş ve kök nedenler ayrıntılı olarak tartışılmıştır. Daha sonra süreç kararlılığını incelemek için kontrol grafikleri oluşturulmuştur. Ek olarak, iyileştirme öncesi süreç yetenek analizi gerçekleştirilmiştir. Su sızıntısı sorununun temel nedenleri arasında hem enjeksiyon kalıplama hem de titreşim kaynak işlemlerinin olduğu belirlenmiştir. Bu nedenle yapılan iyileştirme çalışmaları arasında kalıp bakımı ve temizliği ile kaynak makinesinde özel fikstür kullanımı yer almıştır. İyileştirmeler yapıldıktan sonra son kontrol grafikleri oluşturulmuş ve süreç yeterlilik analizleri yeniden gerçekleştirilmiştir. Sonuçlar, iyileştirilmiş sürecin kontrol altında olduğunu ve süreç kapasitesinin önemli ölçüde arttığını ortaya koymuştur. Ayrıca yapılan iyileştirmelerin istatistiksel anlamlılığı ve önemi hipotez testleri ile doğrulanmıştır. İyileştirmeler sürdürülebilirlik için standartlaştırılmıştır. Son olarak, ek bir düzeltici faaliyet olarak, önceki manuel sistemin yerine yeni bir otomatik sızıntı test sistemi tasarlanmış ve kullanılmıştır. Bu iyileştirme aynı zamanda müşteriye sevk edilen hatalı su tankı miktarını da azaltmıştır.

**Anahtar kelimeler:** Ev aletleri, Kalite iyileştirme, Plastik enjeksiyon kalıplama, İstatistiksel süreç kontrolü, Titreşim kaynağı

**GRAPHICAL ABSTRACT**

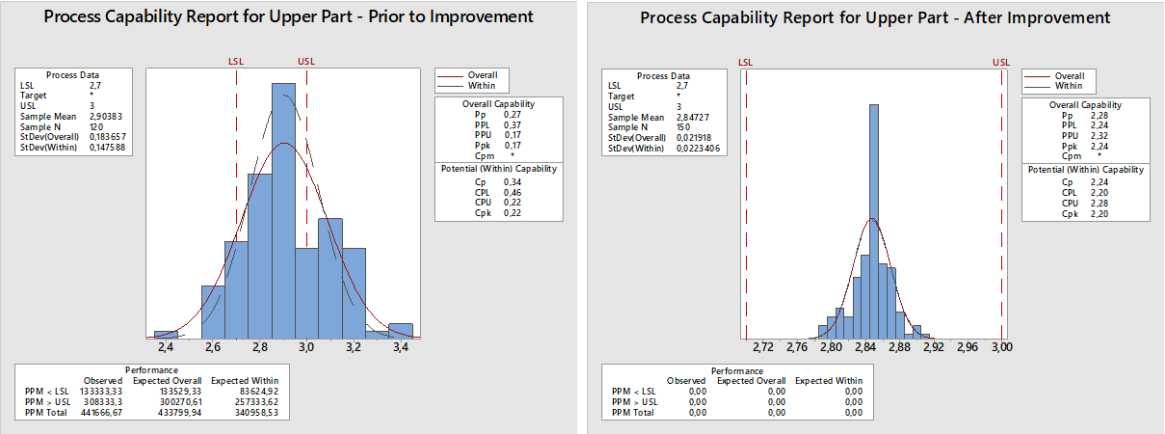


## 1. Introduction

A wide range of plastic goods are utilized at every aspect of our life. Accordingly, plastic manufacturing is among the most important branches of industry [1]. The plastic molding industry is a large and diversified one that produces many industrial and consumer products. Manufactured plastic products are used in different areas, including automotive, building materials, household appliances, electronics, disposable items and medical products. The production of plastic parts that have complex forms can be carried out at low cost by injection molding process [2]. Therefore, injection molding is frequently used in the production of a wide range of plastic parts and components [3].

In injection molding process, plastic pellets are melted, injected into a cavity and then cooled into a new solid form. However, traditional manufacturing techniques for plastic products, such as injection molding, can limit the shape of components. Hence, it becomes necessary to join components to create more complex geometries. Vibration welding is among the techniques of joining components [4]. Vibration welding provides a robust process for physically joining thermoplastics to construct complex hollow final products from simpler injection-molded components without utilization of an external heat source, adhesive, or mechanical fastener [5]. Therefore, the weld interface is composed of the same material as the welded parts. Advantages of vibration welding include relatively short cycle times and energy efficiency [6]. In vibration welding, plastic components are heated by an oscillating friction movement of the joining surfaces, then plasticized and consequently welded together. Therefore, the joining of three-dimensional components is a challenge for vibration welding, as the components can be lifted off by the linear movement and the surfaces do not plasticize sufficiently [4].

Considering both injection molding and its complementary process - vibration welding, achieving the required quality level of manufactured parts is critical. Accordingly, in this study, the goal is to decrease a particular defect seen on molded-and-vibration-welded plastic products. In order to achieve this, condenser dryer water tanks, which are manufactured through plastic injection molding and vibration welding processes, were examined. Water leakage problem encountered on these tanks were aimed to be minimized through statistical process control techniques, including workflow, control charts, process capability analysis, cause-and-effect diagram and hypothesis testing.

The remainder of the paper is as follows, it introduces the product, continues with the determination of the problem and workflow, then discusses about the root causes in detail, provides the analyses regarding initial and final process stability and capability, and finally concludes with significance of the improvement.

## 2. Introducing the Product

A clothes dryer machine, also called as tumble dryer, is a white good which removes moisture from textile products such as clothes and bedding, after they are washed. There are two types of dryers, vented tumble dryers and condenser tumble dryers. In a condenser dryer the humid hot air is transferred to a condensing chamber where it is condensed into water. Then, this condensed water is collected and stored in a container, known as water tank, which is located at the bottom of the dryer. Therefore, a condenser dryer does not pump humid air out to its environment. In condenser dryers it is critical that water tank should be manufactured appropriately and does not leak. Water tank consists of two parts, upper and lower covers, shown in Figure 1. These parts are manufactured via plastic injection molding and assembled via vibration welding process.

Figure 1. Water tank upper and lower covers

## 3. Determination of the Problem

Dryer water tanks, which are manufactured in the study plant, are sent to a large white goods manufacturer, i.e. its customer company. Water leakage of water tanks was seemed as a minor issue, until this problem was encountered in 300 water tanks, out of 6000, that are manufactured and sent to the customer. The customer company returned the whole batch asking for a compensation of $7500. This returned batch has cost the study plant a total of $12500, in which $7500 was for compensation and $5000 was for labor and energy. Obviously, the problem of water leakage in the water tank component is definitely not desired by the customer company and by end-users. Therefore, it was decided to initiate an improvement study to eliminate this problem and also to design a new automation system for water leaking test, which was conducted manually, as a quick action plan.

## 4. Analyses and Results

### *4.1. Workflow*

The water tank production workflow starts with inspection of incoming raw material, i.e. plastic pellets, then continues with feeding of these material into production lines, in which injection molding process takes place. Injection molding, through which a wide range of products are manufactured, is the most frequently used process for production of plastic components. In the injection molding process, initially plastic pellets are placed in the feeder hopper, then the plastic is melted in the injection barrel and finally, hot melted plastic is pushed into the mold, where it cools and solidifies into the final part. After both upper and lower parts of the water tank are manufactured via injection molding, visual audit is conducted. Then, vibration welding process takes place in order to join the two components. Vibration welding uses heat generated by friction at the interface of two components to produce melting in the interfacial area. When the surfaces-to-be-joined are heated, they are plasticized and subsequently welded together.

After main assembly takes place via vibration welding, the water tanks are subject to water leak testing. Finally, the tanks that pass the leak testing are sent to final assembly where final ring cap is assembled. Packed components are then shipped to the customer. The process workflow is given in Figure 2.

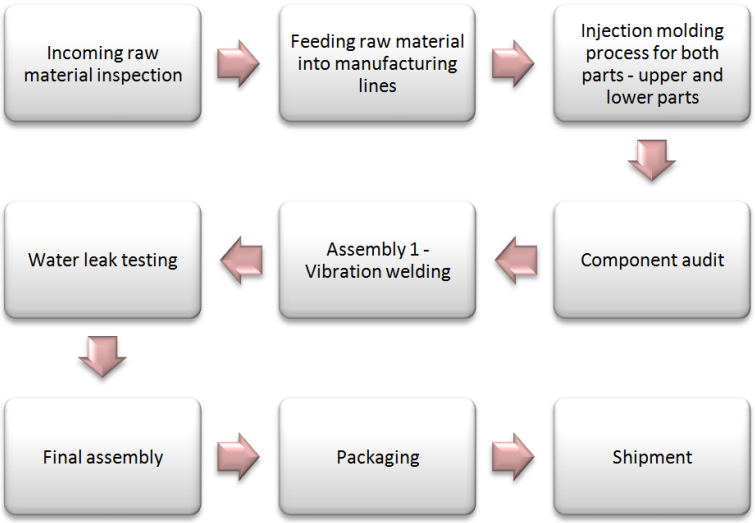


Figure 2. Process workflow

### *4.2. Cause-and-Effect Diagram*

The cause-and-effect diagram presenting the potential causes of water tank leakage was created via Minitab (Figure 3). Water tank leakage issue can be attributed to causes related to machine, method, operator and material.

Machine related causes may be due to vibration welding machine as well as due to injection molding machine. When *vibration welding machine* related causes were examined it was seen that there was only one welding machine in the manufacturing plant, whereas, frequent model changes of produced parts were required. However, standard fixtures were used instead of custom ones for each

different part-to-be-welded to save changeover time. For this reason, about 10 to 15 parts were scrapped whenever the model of the produced part was changed. Usage of standard fixtures were also causing slippage of the parts-to-be-welded which caused leakage problem. In addition, in order to adjust the fixture to the size of the parts-to-be-welded, a rubber band was attached to support the parts during vibration welding. It was examined that the rubber band, which wears out over time, causes dimensional differences in the final product produced leading to leakage problem.

On the other hand, when *injection molding machine* was examined it was seen that the ejector system was losing its required angle as it pushed the parts off of the mold. In addition, the molded parts, i.e. water tanks, had incomplete and partial fillings due to mold being old and its poor maintenance.

Regarding both *method* and *operator errors*, it was found that cracks occurred in the welding area of the water tanks produced during welding process due to improper placement of the upper and lower covers of water tanks on the fixture in the welding machine.

Finally, no issues regarding *environment* or *raw material* were found. Therefore, the main causes of water leakage problem were due to vibration welding machine.

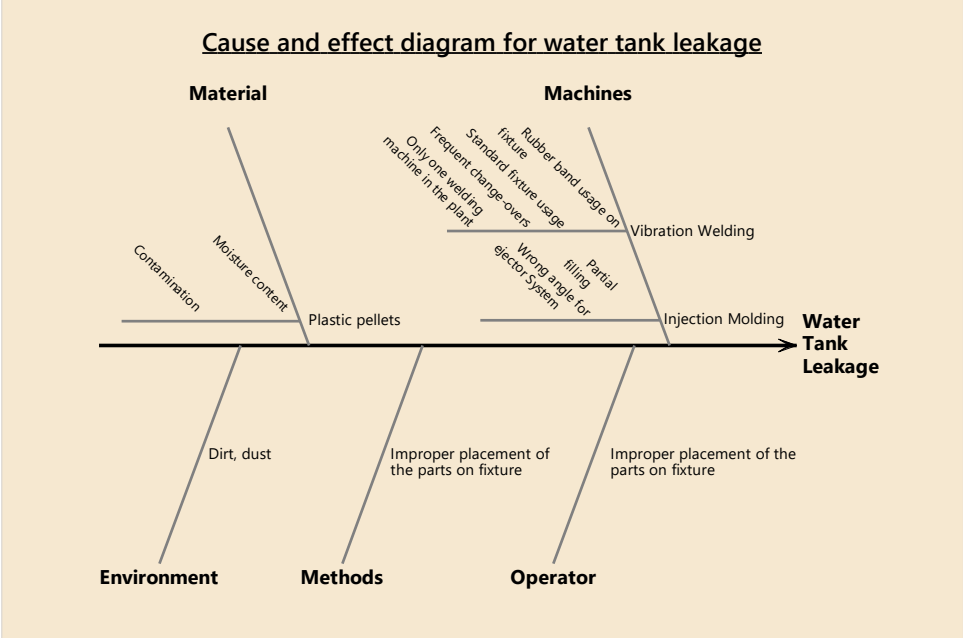


Figure 3. Cause and effect diagram

### *4.3. Initial Control Charts and Process Capability Analysis*

In order to examine the injection molding process, length of the upper part filter area was measured for 10 consecutive hours, for samples of 15 units taken each hour. Then, $\bar{X} - S$ control charts were created via Minitab (Figure 4).

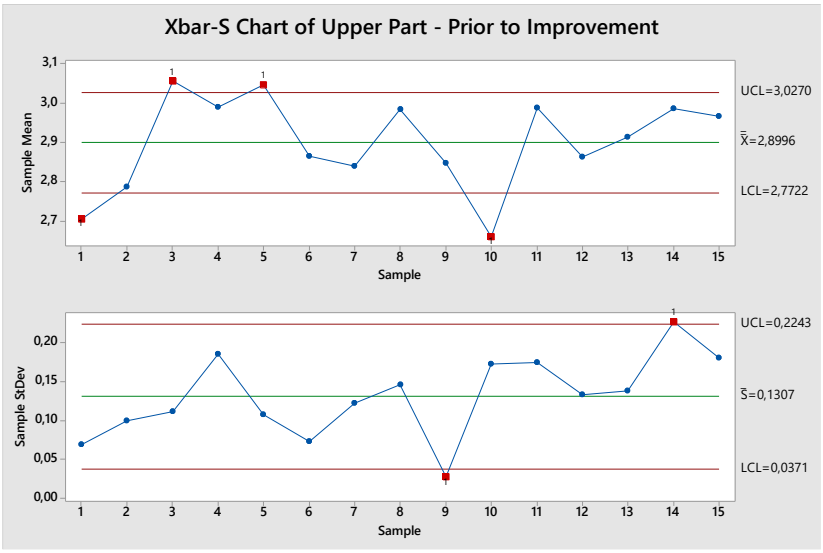


Figure 4. Initial $\bar{X} - S$ control chart

It was determined that 1st, 3rd, 4th and 10th samples were out of control in the $\bar{X}$ chart (Figure 4). It was determined that the 1st sample was the initial sample molded in that shift when machine parameters was not stable, therefore this sample was excluded from the data. Also it was determined that the injection pressure was very low while the 10th sample was being molded. Therefore, 10th sample was also excluded from the data and $\bar{X} - S$ control charts were re-created (Figure 5).

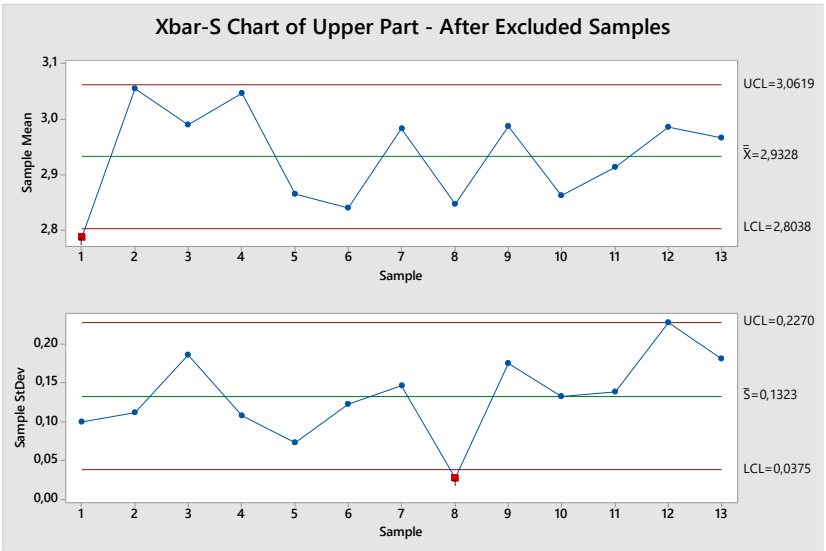


Figure 5. $\bar{X} - S$ control charts after 1st and 10th samples were excluded

After control charts were created for injection molding process, process capability analysis, which assesses the conformity of the process outputs with specification limits, was conducted. The specification limits are 2.70 - 3.00 cm for the length of the upper part filter area.

In order to conduct capability analysis, the data, which was collected for control charts, except for the excluded 1st and 10th samples, was utilized. Therefore, initial process capability analysis was run with a total of 120 measurements. The $C_p$ value, was found to be 0.34 which indicates high variation with respect to specification interval and poor capability for the process (Figure 6). On the

other hand, $C_{pk}$ value was calculated as min($C_{pl} = 0.46$; $C_{pu} = 0.22$)= 0.22, also indicating poor process capability which is not properly centered on the nominal value.

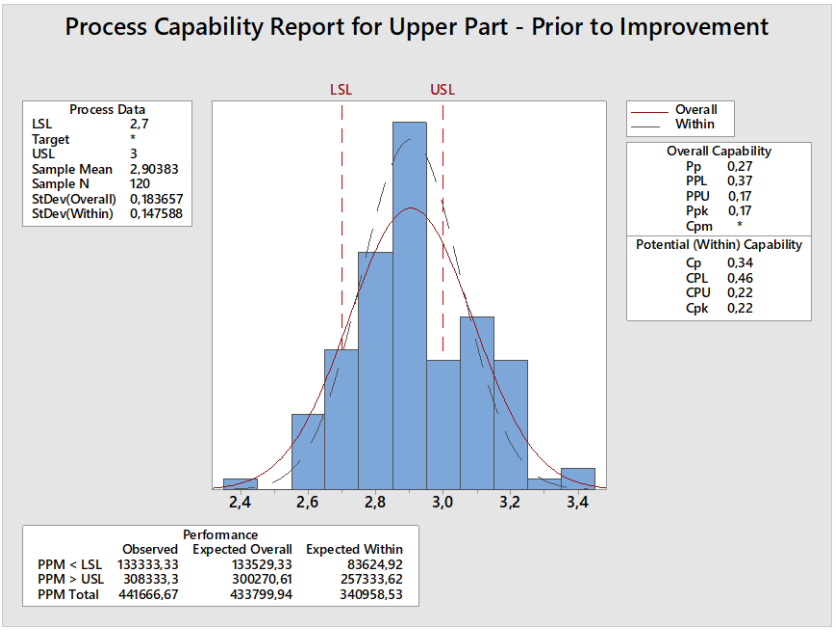


Figure 6. Initial process capability analyses

## 5. Improvement and Discussion

It was determined during root-cause analyses that both injection molding equipment and vibration welding equipment were among the root causes of water leakage problem. Standard fixtures were being used during welding operations to save changeover time. However, this situation resulted in scrapped parts, as well as, slippage of the parts-to-be-welded, which ultimately caused the water leakage problem. In order to eliminate these issues, the fixtures in the vibration welding was planned to be changed in every model change. Therefore, customized fixtures rather than standardized ones were started to be utilized during welding process.

Additionally, a rubber band was being attached to the welding machine to accommodate small dimension changes and to prevent parts from slipping during welding process. However, this band wears out easily and therefore, cannot provide full support for the parts for extended periods. This causes dimensional differences in the final product leading to leakage problem. As an improvement action, standard controls are set in place at the beginning of each welding process to change/renew the rubber band.

Moreover, the ejector system in the injection molding machine failed to run at its required angle as it pushed the parts off of the mold. In addition, the molded parts, i.e. water tanks, had incomplete and partial fillings due to poor mold maintenance. In order to overcome these issues, a detailed mold maintenance was conducted. First, the mold was completely disassembled, cleaned, and greased with new lubricants and inspected for signs of wear. Any part of the mold that was defective or damaged, including ejector pins, was repaired. Then, the mold was reassembled and a final systems check was run. In addition, shorter mold cleaning and greasing cycles were planned for proper tool maintenance and general preventative maintenance was scheduled. Also, it was planned that the molding machine operator would check the ejector system prior to each injection process initiates.

Finally, because cracks occurred on the water tanks due to improper placement of the upper and lower covers of water tanks on the fixture in the welding machine, welding operators had refreshment training on the welding machine components.

### *5.1. Hypothesis Testing for Significance of Improvement*

After the improvements, i.e. detailed injection molding equipment maintenance, operator training efforts, and fixtures changes in the vibration welding process, were in place, the significance of these improvements were tested. Depending on these improvements, the study company ensures its customers that the water leakage defect rate for the water tanks that they manufacture will not be more than 1%. In order to test this claim, 300 randomly selected water tanks were examined. It was observed that only 2 of the water tanks examined had leakage problem. Hypotheses tests were conducted at 0.01 significance level. The null and alternative hypotheses for this test are:

$H_0: p' \leq 0.01$

$H_a: p' > 0.01$

where,

$n = 300$

$x = 2\ (defective\ water\ tank\ quantity)$

$p_0 = 0.01$

$\hat{p} = 2/300 = 0.006667$

$\alpha = 0.01$

$z_{table} = -2.325$

$$z_{calculated} = \frac{\hat{p} - p_0}{\sqrt{p_0(1 - p_{0)}/n}} = -0.58$$

Since $z_{calculated} = -0.58 > z_{table} = -2.325$, we fail to reject $H_0$ at the 0.01 significance level. Accordingly, p-value is 0.719 > α=0.01 level as seen in the Minitab output (Table 1). This indicates that the claim assuring less than 1% defect rate regarding water leakage in the water tanks was met. Therefore, the improvements made were successful.

Table 1. Minitab output for the hypothesis test of significance of improvement

Test of p = 0.01 vs p > 0.01

| Sample | X | n | Sample p | Z-value | p-value |
|---|---|---|---|---|---|
| 1 | 2 | 300 | 0.006667 | -0.58 | 0.719 |

### *5.2. Final Control Charts and Process Capability Analysis*

After improvements took place, control charts were re-created with 15 samples, which comprised 10 units each. As seen in Figure 7, the injection molding process was in control with no special causes.

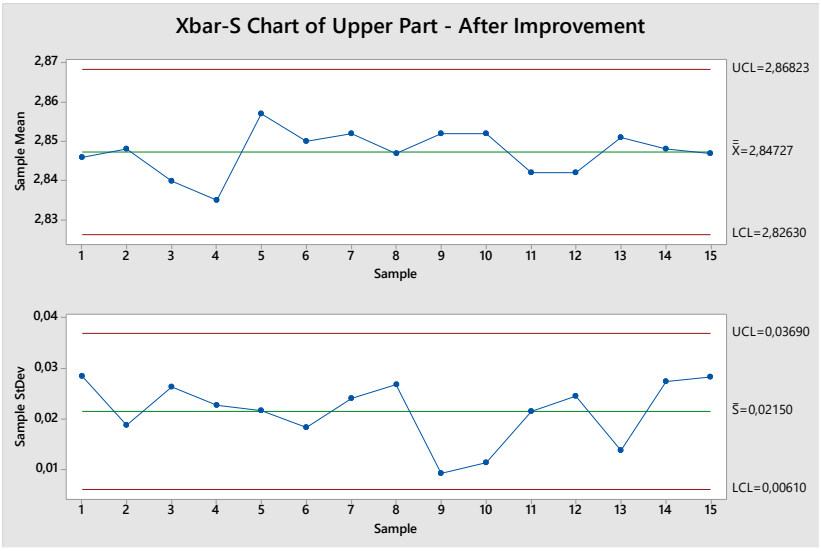


Figure 7. Final $\bar{X} - S$ control charts - after improvement

In addition, final process capability analysis was conducted to determine the level of improvement (Figure 8). The results revealed the fact that both $C_p$ and $C_{pk}$ values were improved. $C_p$ value increased to 2.24 indicating very small variation with respect to specification interval, whereas, $C_{pk}$ value was increased to 2.20 indicating a perfectly centered process on the nominal value. Since both indices were above 1.33, the required value, final process was capable of meeting specifications.

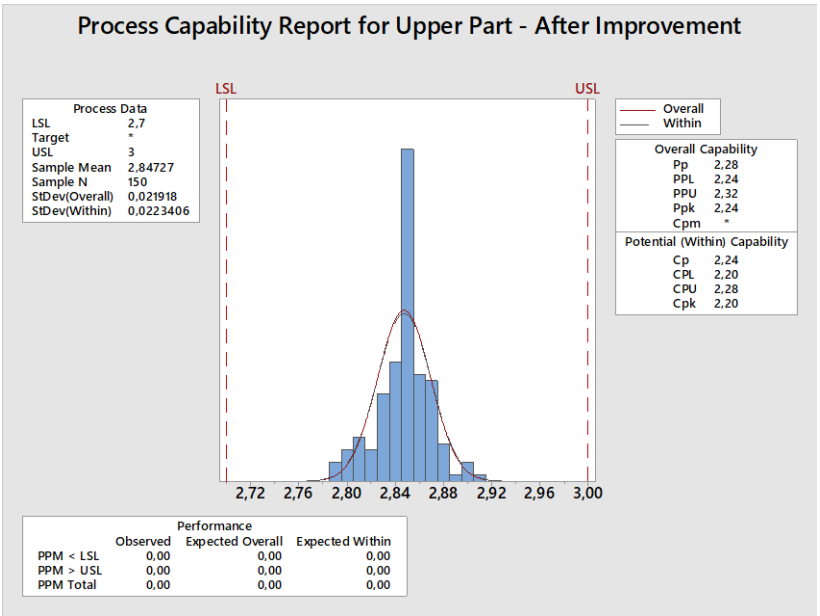


Figure 8. Final process capability analyses - after improvement

### *5.3. Additional Improvement in Water Leak Testing*

In addition to improvements made on the injection molding and vibration welding processes, water leak testing process was also examined. Leak testing consists of mainly four steps; i) placement of the water tank on the test machine, ii) the tank is filled with water up to the max level on the tank, iii) if no water leakage was detected, water is drained through drainage hose and iv) the water tank is unloaded from the test machine. The leak testing was performed manually and some operator-related errors were determined after assessments.

It was determined that water level in the tank during the leak testing was below the max level, i.e. the specified level. This problem occurred due to the early removal of the filling hose from the tank by the operator. Also machine pressure-related errors existed. In addition, the water tank was being scratched while testing due to manual operations.

Moreover, at some times, leakage was failed to be detected due to the water remaining in the hose. This remaining water in the hose were spilled on the floor by mistake and it could not be understood which product had water leakage problem (Figure 9).

Figure 9. Water spill under the manual leak testing area

Finally, 100% leak testing could not be performed on all water tanks, because filling and draining of water from the tanks were performed at the same station. Therefore, some water tanks were being packaged and shipped to the customer without being tested due to confusion.

In order to prevent all these above mentioned problems due to manual operations, a new water leak test automation system was designed and started to be utilized. With this newly designed automated testing system, the primary purpose is to conduct 100% inspection on the final products and to ship them to the customer with zero defects (Figure 10).

Figure 10. Automated leak testing system

18 water tanks can be attached to the newly designed system. In this system, while filling operation is carried out in a water tank at the same time, drainage operation can be performed in a different water tank. Also, the problem of water pump pressure has been resolved.

With the new water leak testing automation system, the dependency on manual operations is eliminated. In the previous system, because the hose was manually attached and removed, water remaining within the hose used to spill on the floor and created a confusion about the leakage problem. This problem has been completely resolved by means of special plates in the new water leak test automation system. In the new system, water filling and drainage is done by the machine itself and a sensor is activated and a red light turns on as soon as water drops on the plate. After the red light turns on, the machine automatically stops and does not initiate until a new tank is installed and the plate is fully cleaned.

## 6. Conclusion

In this study, dryer water tanks, which are manufactured via plastic injection molding and vibration welding processes, were examined and water leakage problem were minimized through statistical process control techniques. First, the product was introduced for thorough understanding. Then, the cost of water leakage problem for the manufacturing company was provided and the criticality of the issue was put forward. After the determination of the problem, water tank manufacturing steps were explained as a process flow. Then, the cause-and-effect diagram depicting the potential causes of water tank leakage was constructed and the potential as well as the root causes were discussed in detail. Then control charts were created to determine whether the process was in control or not. In addition, initial process capability analysis was conducted through which poor process capability was revealed.

It was determined that both injection molding and vibration welding processes were among the root causes of water leakage problem. Therefore, efforts were made, such as mold maintenance and cleaning, and usage of custom fixtures on the welding machine, to improve these processes. After improvements took place final control charts and process capability reports were re-created. Results indicated that the improved molding process was stable and the capability of the process was enhanced considerably. Besides, the significance of the improvements made were confirmed through hypothesis testing. The improvements were standardized for sustainable achievement. Ultimately, as an additional corrective action, a new automated system for leakage testing was designed and started to be utilized as a replacement for the previous manual system. This action also decreased the amount of defective products shipped to the customer.

Plastic injection molding as well as vibration welding are among the most prominent processes across many industries. Accordingly, a wide variety of products are manufactured through these processes. Therefore, further improvement efforts, such as design of experiments, encompassing various other products can be achieved in both plastic injection molding and vibration welding processes.

**Peer-review:** Externally peer - reviewed.

**Author contributions:** Concept M.U.; Data Collection &/or Processing - M.U.; Literature Search - M.U.; Writing - M.U.

**Conflict of Interest:** No conflict of interest was declared by the author.

## References

[1] Desai, D. and Prajapati, B. N. (2017). Competitive advantage through Six Sigma at plastic injection molded parts manufacturing unit. *International Journal of Lean Six Sigma*, *8*(4), 411-435. Doi: https://doi.org/10.1108/IJLSS-06-2016-0022

[2] Khavekar, R., Vasudevan, H. and Modi, B. (2017). A comparative analysis of Taguchi methodology and Shainin system DoE in the optimization of injection molding process parameters. In *IOP Conference Series: Materials Science and Engineering* (Vol. 225, No. 1, p. 012183). IOP Publishing.

[3] Maged, A., Haridy, S., Kaytbay, S. and Bhuiyan, N. (2019). Continuous improvement of injection moulding using Six Sigma: case study. *International Journal of Industrial and Systems Engineering*, *32*(2), 243-266. Doi: https://doi.org/10.1504/IJISE.2019.10021839

[4] Vogtschmidt, S., Fiebig, I. and Schoeppner, V. (2020). Vibration welding of components with angled areas in the direction of vibration. *Welding in the World*, *64*(11), 1843-1853. Doi: https://doi.org/10.1007/s40194-020-00964-6

[5] Patham, B. and Foss, P. H. (2011). Thermoplastic vibration welding: Review of process phenomenology and processing–structure–property interrelationships. *Polymer Engineering & Science*, *51*(1), 1-22.

[6] Troughton, M. J. (2008). *Handbook of plastics joining: a practical guide*. William Andrew: Norwich, NY, USA. Doi: https://doi.org/10.1016/B978-0-8155-1581-4.50005-

# Molecular Docking Analysis of N-[2-(3-Methylthio(1,2,4-Thiadiazol-5-Ylthio))Acetyl] Benzamide Molecule with Integrin and DNA

Aliye Demet DEMİRAG[1,4], Sefa CELİK[2], Dogan OZEN[3], Aysen E. OZEL[2], Sevim AKYUZ[5]

[1] Yeditepe University, Vocational School, Internet and Network Technologies Department, 34755, Istanbul
[2] Istanbul University, Faculty of Science, Department of Physics, Vezneciler, 34134, Istanbul
[3] Yeditepe University, Vocational School, Automotive Technologies Department, 34755, Istanbul
[4] Istanbul University, Institute of Graduate Studies in Sciences, 34452, Istanbul
[5] Istanbul Kultur University, Faculty of Science and Letters, Department of Physics, 34156, Istanbul
**Corresponding author, e-mail**: demet.demirag@yeditepe.edu.tr

Submission Date: 05.10.2021 Acceptation Date: 29.11.2021

**Abstract -** The most stable structure of the N-[2-(3-Methylthio(1,2,4-thiadiazol-5-ylthio))acetyl] benzamide molecule ($C_{12}H_{11}N_3O_2S_3$) have been determined by conformational analyses using semi-experimental AM1 calculations. The obtained most stable conformation has been used as the initial data of N-[2-(3-Methylthio(1,2,4-thiadiazol-5-ylthio))acetyl] benzamide in molecular docking analysis. Molecular docking studies of the title molecule with DNA and target protein $\alpha_5\beta_1$ integrin revealed the binding affinities as $\Delta G$ = -7.4 and -7.7 kcal/mol, respectively. The binding sites of the target protein integrin and DNA and the interactions of the ligand-integrin and ligand-DNA complexes have been determined, which play an important role in anticancer studies. The 3D docked structures of the investigated molecule in target molecules and the interacted groups of ligand receptor complexes were calculated and shown in figures.

**Keywords:** Benzamide molecule, Target protein integrin, Molecular docking, DNA, Anticancer properties

## 1. Introduction

Benzamide appears as an off-white crystals or powder [1]. It is a flammable substance, and is incompatible with strong oxidizing agents and strong bases and emits nitrogen oxides, carbon monoxide and carbon dioxide in combustion and thermal decomposition [2]. The benzamide molecule is not planar because it exhibits an angle of 26 degrees with the amide group and the benzene ring [3]. The amide group conformation may result from the repulsive interaction between the hydrogen atoms of the amide group and the atoms of the aromatic ring [4].

Kwolek et al. have produced PBA, a commercialized homopolymer with the simplest chemical structure among p-aramids [5]. PBA has p-aminobenzoic acid, which has condensed and reacted to generate benzamide on its own. PBA can be obtained directly by dissolving sulfinyl aminobenzoyl chlorine in an amide solvent such as tetramethylurea with equivalent water [6]. Benzamide is a carbonic acid amide of benzoic acid. It has the general formula RCO-$NH_2$ and belongs to the group of organic chemicals [7].

Benzamide and its derivatives have different pharmacological activities such as anticancer, analgesic, cardiovascular, antimicrobial and other biological activities [7]. For this reason, scientists have done many studies to develop different types of benzamide derivatives. For example, amisulpride and sulpiride, both from the benzamides family, have been employed in medicine and in medical materials [8]. Remoxipride, a new benzamide, has been introduced in 1993. Amidoxime derivatives, which are prodrug forms, have been established to solve bioavailability problems with

amide derivatives created before and amidine derivatives, which are thought to be physiologically beneficial [9].

Other study, radiotracer benzamide derivatives that target melanin for melanoma imaging to diagnose malignant melanoma have been designed [10]. Ren and coworkers have synthesized a benzamide derivative to use as 18F-labeled PET imaging probe that targets primary and metastatic melanotic-melanoma [11].

In a study, docking studies of several anticarcinogenic benziamide derivatives affecting human topoisomerase (I, II) enzymes have been carried out [12]. 4N6, 5N5 for Topo I compounds and 5N3, 5N7 for Topo IIa compounds have all been identified as potential anticancer chemicals [12].

The presence of compounds having pharmacological characteristics separates benzamides from other types. Benzamides have turned out to be more selective and more potent for certain HDACs than for all HDAC grades. Although it appears to inhibit HDAC1, HDAC2, and HDAC3 with high potency, benzamides have been shown to induce P21WAF1 expression, induce cell cycle arrest, activate several proapoptotic genes, and to be cytotoxic in a variety of tumor cell types at micromine concentrations. Additionally, specific benzamide analogues have been shown to induce breast cancer cell differentiation [13]. The HDACI family does not have natural products, however, specific synthetic benzamides play an important role in clinical trials on diseases such as breast cancer and lymphoma [13]. Benzamides such as entinostat and mocetinostat have been used in clinical studies on such diseases [14]. In clinical trials, it has so far passed through HDAC inhibitors and it has been approved by the Food and Drug Administration [15]. These inhibitors are panobinostat, vorinostat, romidepsin, and belinostat have been approved to treat different malignancies. Furthermore, a comprehensive investigation using compounds such as valproic acid, butyrates, givinostat, belinostat, entinostat, and mocetinostat has done, with varying results in clinics [16,17].

As a result, benzamide derivatives are evaluated in different fields, using different methods, and are especially important as bioactive molecules. There are great future prospects for compounds in this area. They play an important role in pioneering drug discovery [18,19]. Studies in this area are carried out by scientists to obtain more comprehensive and effective results.

In this study the most stable conformation of N-[2-(3-Methylthio(1,2,4-thiadiazol-5-ylthio))acetyl] benzamide was identified by conformational analysis. Molecular docking simulation was used to identify the interaction of the most stable conformer of the title molecule with DNA and $\alpha_5\beta_1$ integrin. The binding affinities and interacted sites have been determined.

## 2. Materials and Methods

The study was carried out with the help of the Spartan06 software [20] and the AM1 semiempirical quantum mechanical method [21]. The CAVER software [22] was used to determine the potential binding sites on the surface of the receptors. Molecular docking investigations were done using AutoDock-Vina software on the identified active sites [23].

## 3. Results and Discussions

### 3.1. Structure

The conformational preferences of the N-[2-(3-Methylthio(1,2,4-thiadiazol-5-ylthio))acetyl] benzamide molecule were investigated by performing conformational analysis and computational results revealed the three lowest energy conformations. The molecular models of the obtained the three lowest energy conformers of the N-[2-(3-Methylthio(1,2,4-thiadiazol-5-ylthio))acetyl] benzamide molecule are shown in Figure 1 and their calculated relative energies are tabulated in Table 1. The differences between the energies of the three conformers found are low, and therefore, the contribution of all these conformers to the molecular structure is expected at room temperature.

However, the lowest energy-optimized molecular structure (conformer I) was used in our further studies to determine the activity of the molecule.

**Table 1.** The energies of the three most stable conformers obtained by conformation analysis

| Conformers | Relative energy (kj/mol) |
|---|---|
| ( I ) | 0 |
| ( II ) | 0.24 |
| ( III ) | 2.38 |

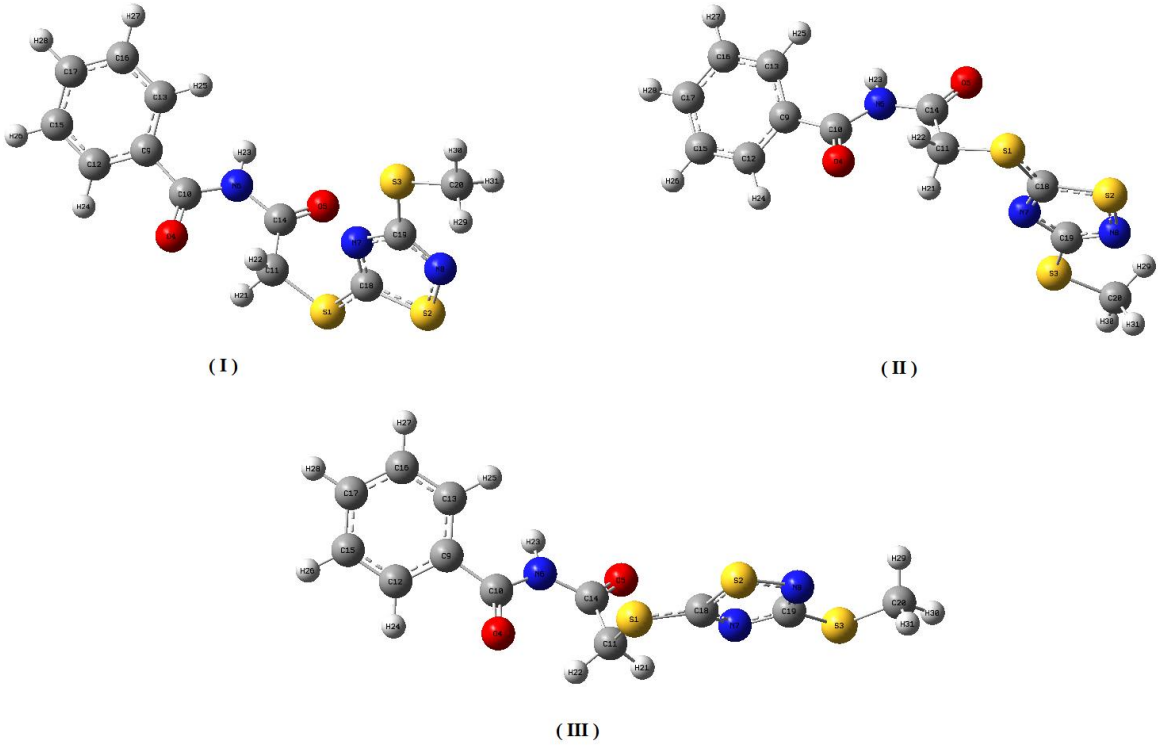


**Figure 1.** The three conformers with the lowest energy, obtained by conformational analysis of the N-[2-(3-Methylthio(1,2,4-thiadiazol-5-ylthio))acetyl] benzamide molecule.

### 3.2. Molecular Docking

Benzamide derivatives are known to have anticancer properties [24]. For this reason, the anticancer property of the title molecule, as benzamide derivative, was investigated by molecular docking simulations. The interactions of the title molecule with DNA and $\alpha_5\beta_1$ integrin were predicted by molecular docking calculations.

Docking analyses were performed by using AutoDockVina [23]. The crystal structure of DNA (PDB ID: 1BNA) was obtained from the protein database [25] and prepared for docking. The water molecules were removed, polar hydrogens were added and the DNA charges of Kollman were determined. The Geistenger technique was used to compute the partial charges of the N-[2-(3-Methylthio(1,2,4-thiadiazol-5-ylthio))acetyl] benzamide molecule and the active region of DNA was determined in grid size 40Å × 40Å × 40Å. The most stable conformer of the N-[2-(3-Methylthio(1,2,4-thiadiazol-5-ylthio))acetyl] benzamide molecule was shown to bind to the nucleic acids DC9, DG10, DC11, and DA17 of DNA through hydrogen bonds and pi-sulfur interactions (See

Figure 2). The binding affinity of the ligand to DNA was found as ΔG = -7.4 kcal/mol. It was revealed that the investigated ligand was docked in a similar active region of DNA given in the literature [26,27]. The interactions between the N-[2-(3-Methylthio(1,2,4-thiadiazol-5-ylthio)] benzamide molecule and the nucleic acids of DNA are given as follows:

Pi-sulfur interaction between DC9 and N-[2-(3-Methylthio(1,2,4-thiadiazol-5-ylthio))acetyl] benzamide molecule with length of 5.56 Å; Hydrogen bond interaction between DG10 and N-[2-(3-Methylthio(1,2,4-thiadiazol-5-ylthio))acetyl] benzamide molecule with length of 2.28 Å; Hydrogen bond interaction between DC11 and N-[2-(3-Methylthio(1,2,4-thiadiazol-5-ylthio))acetyl] benzamide molecule with length of 2.99 Å; Pi-sulfur interaction between DA17 and N-[2-(3-Methylthio(1,2,4-thiadiazol-5-ylthio))acetyl] benzamide molecule with length of 5.68 Å. In the molecular docking study on cyclo(Ala-His) and DNA, by Celik et al., it was reported that cyclic peptide interacted with DC9, DG10, DC11, DG16 and DA17 nucleic acids of DNA through H-bonds. The lengths of these hydrogen bonds were 3.1 Å with DC9, 2.39 Å with DG10, 2.96 Å with DC11, 2.53 and 2.39 Å with DG16, and 2.99 Å with DA17 [27]. In the molecular docking study between 5-chlorouracil (5-FU) molecule and DNA by Akalin et al., 5-FU was interacted with DNA through hydrogen bonds with DG10, DC15 and DG16 [28].

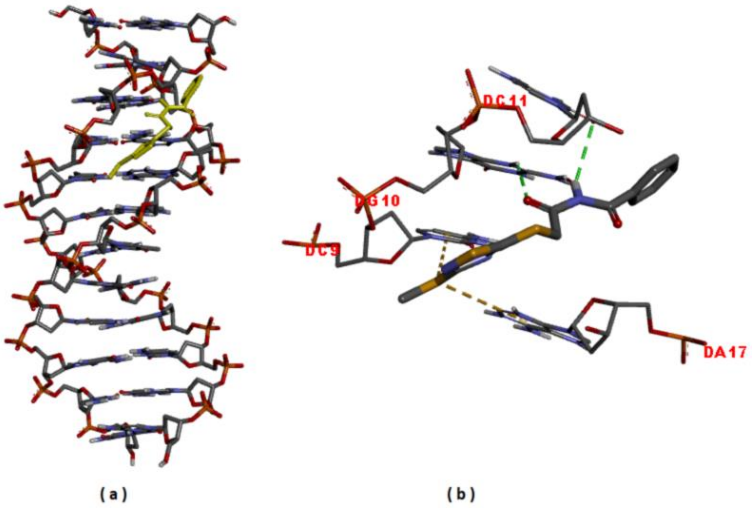


**Figure 2.** Molecular docked model of N-[2-(3-Methylthio(1,2,4-thiadiazol-5-ylthio))acetyl] benzamide with DNA (a) The interactions between the of N-[2-(3-Methylthio(1,2,4-thiadiazol-5-ylthio))acetyl] benzamide and DNA are labeled using coloured dashed lines (b) (ΔG =-7.4 kcal/mol).

Molecular docking studies in target protein $\alpha_5\beta_1$ integrin was performed to examine the anti-proliferation effect of the N-[2-(3-Methylthio(1,2,4-thiadiazol-5-ylthio))acetyl] benzamide for the anticancer activity.

Following the preparations of the $\alpha_5\beta_1$ integrin (PDB ID: 4WK0) and the ligand for the molecular docking analysis, docking simulation was performed on the active site of the target protein [29]. The binding affinity of the investigated ligand was found to be -7.7 kcal/mol. The 3D diagram of the docked N-[2-(3-Methylthio(1,2,4-thiadiazol-5-ylthio))acetyl] benzamide in the active site of $\alpha_5\beta_1$ integrin is shown in Figure 3. The figure also shows the interaction diagrams of the N-[2-(3-Methylthio(1,2,4-thiadiazol-5-ylthio))acetyl] benzamide and $\alpha_5\beta_1$ integrin complex.

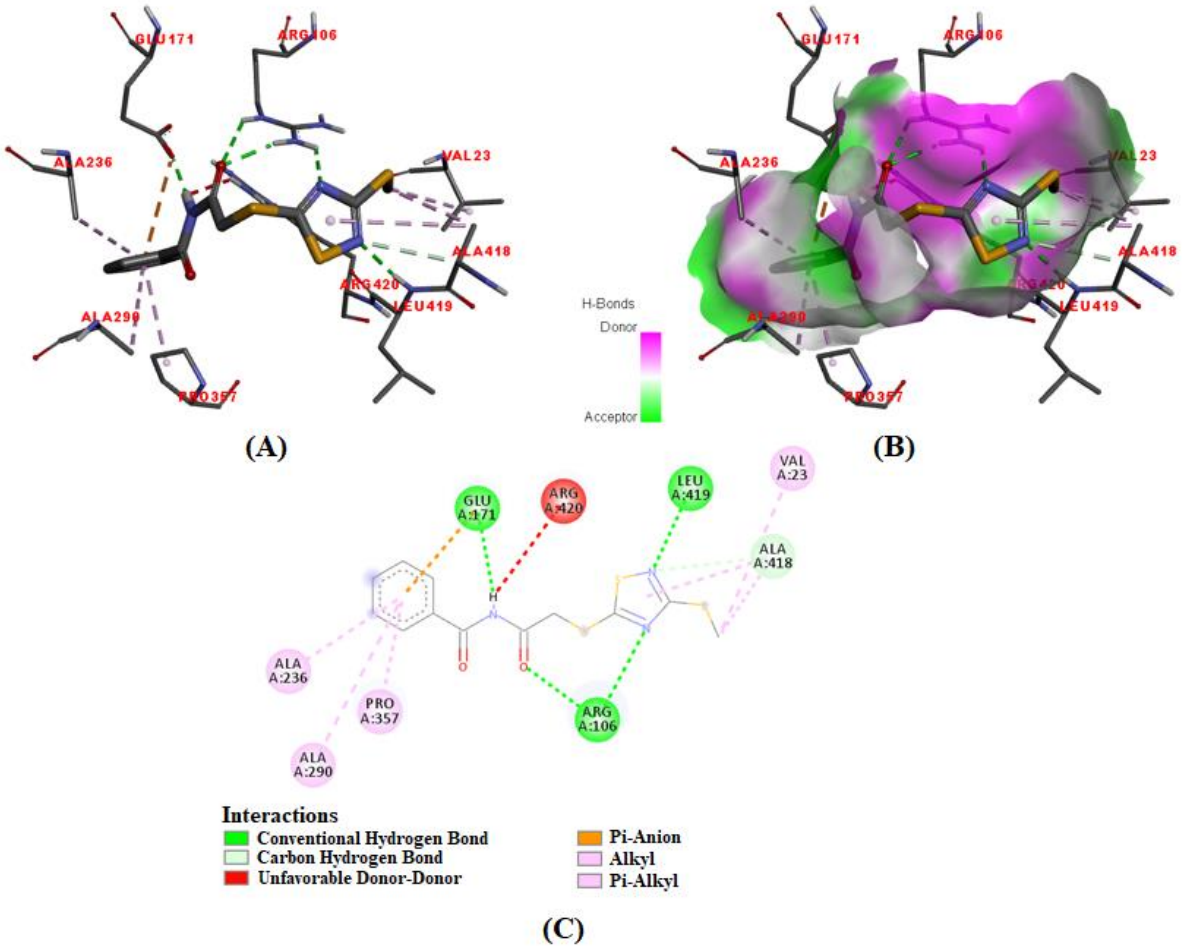


**Figure 3.** Visualization of docking analysis of N-[2-(3-Methylthio(1,2,4-thiadiazol-5-ylthio))acetyl] benzamide binding with $\alpha_5\beta_1$ integrin (-7.7 kcal/mol) (A-C) 3D and 2D representations describing bindings of N-[2-(3-Methylthio(1,2,4-thiadiazol-5-ylthio))acetyl] benzamide with active site of $\alpha_5\beta_1$ integrin (B) visualization of hydrogen bond.

The revealed interactions between N-[2-(3-Methylthio(1,2,4-thiadiazol-5-ylthio))acetyl] benzamide molecule and target protein integrin are as follows: 2.21, 2.48, and 2.98 Å long hydrogen bonds with Arg106; 4.51 Å long alkyl interaction between and Val23; 2.04 Å long hydrogen bond and 4.23 Å long pi-anion interaction with Glu171; 4.97 Å long pi-alkyl interaction with Ala236; 5.33 Å long pi-alkyl interaction with Ala290; pi-alkyl interaction of Pro357 with a length of 4.08 Å; 3.69 Å length alkyl interaction, 5.23 Å length pi-alkyl interaction, 3.61 Å length carbon-hydrogen bond with Ala418; 2.41 Å long hydrogen bond with Leu419; Unfavorable donor-donor interaction with Arg420 at 2.6 Å.

In the case of molecular docking studies between cationic Glu-Gln-Arg-Pro-Arg pentapeptide and the $\alpha_5\beta_1$ integrin, by Gasymov et al., it was found that the pentapeptide interacted with the Phe21, Ser22, Val23, Arg106, Phe168, Glu171, Ser234, Val235, Lys269, Tyr287, Leu355 , Ser417 and Arg420 amino acid residues of integrin, through salt bridge, attractive charge, hydrogen bond, carbon hydrogen bond, unfavorable positive-positive, unfavorable donor-donor interactions [30].

In our study some of the amino acid residues with which the title compound interacted with integrin have been found to be the same as the amino acids with which cationic Glu-Gln-Arg-Pro-Arg pentapeptide interacted. The result indicated that the title molecule bound to the target protein in its active site to which the cationic pentapeptide bound [30].

As a summary, the binding affinities and interactions of N-[2-(3-Methylthio(1,2,4-thiadiazol-5-ylthio))acetyl] benzamide ligand with the target DNA and $\alpha_5\beta_1$ integrin were tabulated in Table 2.

**Table 2.** The binding affinities and the molecular interactions between N-[2-(3-Methylthio(1,2,4-thiadiazol-5-ylthio))acetyl] benzamide and target DNA, and integrin, obtained by molecular docking simulations.

| | **DNA (PDB ID: 1BNA)** | **$\alpha_5\beta_1$ (PDB ID: 4WK0)** |
|---|---|---|
| Docking score (kcal/mol) | -7.4 | -7.7 |
| H.Bonding interaction (distance; Å) | 1- DG10 (2.28)<br>2- DC11 (2.99) | 1- Arg106 (2.21; 2.48; 2.98)<br>2- Glu171 (2.04)<br>3- Leu419 (2.41) |
| Pi-sulfur (distance; Å) | 1- DC9 (5.56)<br>2- DA17 (5.68) | |
| Alkyl (distance; Å) | | 1- Val23 (4.51)<br>2- Ala418 (3.69) |
| Pi-Anion (distance; Å) | | 1- Glu171 (4.23) |
| Pi-Alkyl (distance; Å) | | 1- Ala236 (4.97)<br>2- Ala290 (5.33)<br>3- Pro357 (4.08)<br>4- Ala418 (5.23) |
| Carbon-Hydrogen bond (distance; Å) | | 1- Ala418 (3.61) |
| Unfavorable donor-donor (distance; Å) | | 1- Arg420 (2.6) |

The Molecular Mechanics Poisson-Boltzmann Surface Area (MM/PBSA) and the molecular mechanics generalized Born surface area (MM/GBSA) approaches are reliable binding free energy calculation methods, used to estimate the free energy of binding small ligands to biological macromolecules. Typically, they are based on molecular dynamics simulations of the receptor-ligand complex [31-36]. Due to the importance of both MM/PBSA and MM/GBSA approaches, the interaction free energies of the investigated ligand with DNA and $\alpha_5\beta_1$integrin were calculated using a program developed by Wang [31], which is based on MM/PB(GB)SA approach.

The predicted binding free energy of the N-[2-(3-Methylthio(1,2,4-thiadiazol-5-ylthio))acetyl] benzamide molecule with DNA and with $\alpha_5\beta_1$ integrin were obtained as -13.06 and -20.46 kcal/mol, respectively by using the MM/PB(GB)SA approaches with the GAFF2 and ff14SB force field combination and the GB6 procedure [31].

## 4. Conclusions

A semi-experimental method AM1 was used to analyze the conformational preferences of the N-[2-(3-Methylthio(1,2,4-thiadiazol-5-ylthio))acetyl] benzamide molecule. The docking simulations were performed to reveal the biological activity of the title molecule in its most stable conformer. Since the DNA and integrins are important targets for anticancer drugs, the docking simulations of N-[2-(3-Methylthio(1,2,4-thiadiazol-5-ylthio))acetyl] benzamide molecule were performed with DNA and $\alpha_5\beta_1$ integrin to predict the anticancer activity of the title molecule. The N-[2-(3-Methylthio(1,2,4-thiadiazol-5-ylthio))acetyl] benzamide had binding affinities of -7.4 and -7.7 kcal/mol to DNA and $\alpha_5\beta_1$ integrin, respectively. The ligand N-[2-(3-Methylthio(1,2,4-thiadiazol-5-ylthio))acetyl] benzamide predicted to have strong anti-tumor effects, according to molecular docking simulations.

**Peer-review:** Externally peer - reviewed.

**Conflict of Interest:** No conflict of interest was declared by the authors.

**Financial Disclosure:** The authors declared that this study has received no financial support.

**References**

[1] Dikshith, T. S. S. (2013). Hazardous chemicals: safety management and global regulations. CRC press.

[2] Vincoli, J. W. (1996). Risk management for hazardous chemicals (Vol. 1). CRC Press.

[3] Penfold, B. R., & White, J. C. (1959). The crystal and molecular structure of benzamide. Acta Crystallographica, 12(2), 130-135.

[4] Huc, I. (2004). Aromatic oligoamide foldamers. European Journal of Organic Chemistry, 2004(1), 17-29.

[5] Kwolek, S. L., Morgan, P. W., Schaefgen, J. R., & Gulrich, L. W. (1977). Synthesis, anisotropic solutions, and fibers of poly (1, 4-benzamide). Macromolecules, 10(6), 1390-1396.

[6] Abe, Y. (2012). Polymer Science: A Comprehensive Reference, Lyotropic Polycondensation including Fibers, 469–495. doi:10.1016/B978-0-444-53349-4.00150-3.

[7] Asif, M. (2016). Pharmacological potential of benzamide analogues and their uses in medicinal chemistry. Modern Chemistry & Applications, 4(4), 1000194.

[8] Kreinin, A., Novitski, D., & Weizman, A. (2006). Amisulpride treatment of clozapine-induced hypersalivation in schizophrenia patients: a randomized, double-blind, placebo-controlled cross-over study. International clinical psychopharmacology, 21(2), 99-103.

[9] Ovdiichuk, O. (2016). New Variety of Pyridine and Pyrazine-Based Arginine Mimics: Synthesis, Structural Study and Preliminary Biological Evaluation (Doctoral dissertation, Université de Lorraine).

[10] Rouanet, J., Quintana, M., Auzeloux, P., Cachin, F., & Degoul, F. (2021). Benzamide derivative radiotracers targeting melanin for melanoma imaging and therapy: Preclinical/clinical development and combination with other treatments. Pharmacology & Therapeutics, 107829.

[11] Ren, G., Miao, Z., Liu, H., Jiang, L., Limpa-Amara, N., Mahmood, A & Cheng, Z. (2009). Melanin-targeted preclinical PET imaging of melanoma metastasis. Journal of Nuclear Medicine, 50(10), 1692-1699.

[12] Yilmaz, S., Ataei, S., & Yildiz, İ. (2020). Molecular docking studies on some benzamide derivatives as topoisomerase inhibitors. Journal of Faculty of Pharmacy of Ankara University, 44(3), 470-480.

[13] Bishayee, A., & Bhatia, D. (Eds.). (2018). Epigenetics of cancer prevention (Vol. 8). Academic Press.

[14] Gerson, S. L., Caimi, P. F., William, B. M., & Creger, R. J. (2018). Pharmacology and molecular mechanisms of antineoplastic agents for hematologic malignancies. In Hematology (pp. 849-912). Elsevier.

[15] Mottamal, M., Zheng, S., Huang, T. L., & Wang, G. (2015). Histone deacetylase inhibitors in clinical studies as templates for new anticancer agents. Molecules, 20(3), 3898-3941.

[16] Garmpis, N., Damaskos, C., Garmpi, A., Valsami, S., & Dimitroulis, D. (2019). Pharmacoepigenetics of Histone Deacetylase Inhibitors in Cancer. In Pharmacoepigenetics (pp. 501-

521). Academic Press.

[17] Vilwanathan, R., Chidambaram, A., & Chidambaram, R. K. (2019). Pharmacoepigenetics: Novel Mechanistic Insights in Drug Discovery and Development Targeting Chromatin-Modifying Enzymes. In Pharmacoepigenetics (pp. 437-445). Academic Press.

[18] Tumer, T. B., Onder, F. C., Ipek, H., Gungor, T., Savranoglu, S., Tok, T. T., ... & Ay, M. (2017). Biological evaluation and molecular docking studies of nitro benzamide derivatives with respect to in vitro anti-inflammatory activity. International immunopharmacology, 43, 129-139.

[19] Martinez-Mayorga, K., Peppard, T. L., López-Vallejo, F., Yongye, A. B., & Medina-Franco, J. L. (2013). Systematic mining of generally recognized as safe (GRAS) flavor chemicals for bioactive compounds. Journal of agricultural and food chemistry, 61(31), 7507-7514.

[20] Shao, Y., Molnar, L. F., Jung, Y., Kussmann, J., Ochsenfeld, C., Brown, S. T., ... & DiStasio Jr, R. A. (2006). Advances in methods and algorithms in a modern quantum chemistry program package. Physical Chemistry Chemical Physics,8(27), 3172-3191.

[21] Devar, M.J.S.;Zoebisch, E.G.; Healy, E.F.; Stewart, J.J.P. (1985). AM1: A new General purposequantum mechanical molecular model. Journal of the American Chemical Society,107, 3902-3909.

[22] Jurcik, A.; Bednar, D.; Byska, J.; Marques, S.M.; Furmanova, K.; Daniel, L.;... Pavelka, A. (2018). CAVER Analyst 2.0: analysis and visualization of channels and tunnels in protein structures and molecular dynamics trajectories. Bioinformatics, 34, 3586-3588.

[23] Trott, O.; Olson, A.J. (2010). AutoDock Vina: Improving the speed and accuracy of docking with a new scoring function, efficient optimization, and multithreading. Journal of Computational Chemistry,31, 455-461.

[24] El-Hashash, M.A.E.M., Salem, M. S., & Al-Mabrook, S.A.M. (2018). Synthesis and anticancer activity of novel quinazolinone and benzamide derivatives. Research on Chemical Intermediates, 44(4), 2545-2559.

[25] Drew, H. R., Wing, R. M., Takano, T., Broka, C., Tanaka, S., Itakura, K., &Dickerson, R. E. (1981). Structure of a B-DNA dodecamer:Conformation and dynamics.Proceedings of the National Academy ofSciences,78(4), 2179–2183.

[26] Arif, R., Rana, M., Yasmeen, S., Khan, M. S., Abid, M., & Khan, M. S. (2020). Facile synthesis of chalcone derivatives as antibacterial agents: Synthesis, DNA binding, molecular docking, DFT and antioxidant studies. Journal of Molecular Structure, 1208, 127905.

[27] Celik, S., Yilmaz, G., Ozel, A. E., & Akyuz, S. (2020). Structural and spectral analysis of anticancer active cyclo (Ala–His) dipeptide. Journal of Biomolecular Structure and Dynamics, 1-13.

[28] Akalin, E., Celik, S., & Akyuz, S. (2020). Molecular Modeling, Dimer Calculations, Vibrational Spectra, and Molecular Docking Studies of 5-Chlorouracil. Journal of Applied Spectroscopy, 86(6), 975-985.

[29] Xia, W., & Springer, T. A. (2014). Metal ion and ligand binding of integrin α5β1. Proceedings of the National Academy of Sciences, 111(50), 17863-17868.

[30] Gasymov, O. K., Celik, S., Agaeva, G., Akyuz, S., Kecel-Gunduz, S., Qocayev, N. M., ... & Aliyev, J. A. (2021). Evaluation of anti-cancer and anti-covid-19 properties of cationic pentapeptide Glu-Gln-Arg-Pro-Arg, from rice bran protein and its d-isomer analogs through molecular docking simulations. Journal of Molecular Graphics and Modelling, 108, 107999.

[31] Wang, Z., Wang, X., Li, Y., Lei, T., Wang, E., Li, D., ... & Hou, T. (2019). farPPI: a webserver for accurate prediction of protein-ligand binding structures for small-molecule PPI inhibitors by

MM/PB (GB) SA methods. Bioinformatics, 35(10), 1777-1779.

[32] Hao, G. F., Jiang, W., Ye, Y. N., Wu, F. X., Zhu, X. L., Guo, F. B., & Yang, G. F. (2016). ACFIS: a web server for fragment-based drug discovery. Nucleic acids research, 44(W1), W550-W556.

[33] Hao, G. F., Wang, F., Li, H., Zhu, X. L., Yang, W. C., Huang, L. S., ... & Yang, G. F. (2012). Computational discovery of picomolar Q o site inhibitors of cytochrome bc 1 complex. Journal of the American Chemical Society, 134(27), 11168-11176.

[34] Yang, J. F., Wang, F., Jiang, W., Zhou, G. Y., Li, C. Z., Zhu, X. L., ... & Yang, G. F. (2018). PADFrag: a database built for the exploration of bioactive fragment space for drug discovery. Journal of chemical information and modeling, 58(9), 1725-1730.

[35] Cheron, N., Jasty, N., & Shakhnovich, E. I. (2016). OpenGrowth: an automated and rational algorithm for finding new protein ligands. Journal of medicinal chemistry, 59(9), 4171-4188.

[36] Wang, E., Sun, H., Wang, J., Wang, Z., Liu, H., Zhang, J. Z., & Hou, T. (2019). End-point binding free energy calculation with MM/PBSA and MM/GBSA: strategies and applications in drug design. Chemical reviews, 119(16), 9478-9508.

**Open Journal of Nano**
(2021) 6–2

# Fabrication of Mullite Reinforced $Y_2O_3$ Added $ZrO_2$ Ceramics and Characterization of These Composites

*[1]Mehmet Akif Hafızoğlu, [2]Tahsin Boyraz, [3]Ahmet Akkuş

[1]Dicle University, Faculty of Engineering, Department of Mechanical Engineering, Diyarbakır, Turkey.
[2]Sivas Cumhuriyet University, Faculty of Engineering, Department of Metallurgical and Materials Engineering Sivas, Turkey.
[3]Sivas Cumhuriyet University, Faculty of Engineering, Department of Mechanical Engineering Sivas, Turkey.
* Corresponding author, e-mail: makif.hafizoglu@dicle.edu.tr

Submission Date: 01.12.2021 Acceptation Date: 25.12.2021

**Abstract** - Mullite ($3Al_2O_3.2SiO_2$) and 3 mol% yttria added zirconia (3 mol% $Y_2O_3$ - 97 mol% $ZrO_2$) powders by conventional ceramic production method. We prepared the mixtures in acetone environment by mechanical alloying method. To synthesize mullite, we prepared $Al_2O_3$ and $SiO_2$ powders mixture with stoichiometric proportions and fired in air at 1600 $^oC$ for 3 h. And we fired yttria added zirconia composites at 1300 $^oC$ for 2 h. Thus, yttria - zirconia and mullite composite phases were obtained and grinding and sieving processes were carried out. Then, we prepared with powder metallurgy method the mullite-free and 10% by weight mullite reinforced yttrium oxide added zirconia mixtures. The powders were pressed by uniaxial pressing after drying. The formed samples were sintered in a high temperature furnace in air conditions for 1 and 5 h at 1500 and 1600 $^oC$ sintering temperatures. Finally, microstructure investigations, phase analysis, 3-point bending, hardness, wear tests, absorption of water, porosity, shrinkage and density results were examined on the composites. For the result, we understand that the amounts of m-$ZrO_2$, t-$ZrO_2$ and c-$ZrO_2$ in the structure varies depending on the sintering temperature and time. So, along with all physical and mechanical properties, especially bending strengths varied. In addition, while the addition of mullite increased the flexural strength, water absorption and porosity values of the composites; It was concluded that hardness, wear, shrinkage and density values decreased.

**Keywords:** Zirconia, Mullite, Yttria, Characterization, Wear.

# Mullit Takviyeli $Y_2O_3$ Katkılı $ZrO_2$ Seramiklerinin İmalatı ve Bu Kompozitlerin Karakterizasyonu

**Öz** - Bu çalışmada, mullit ($3Al_2O_3.2SiO_2$) ve %3 mol itriya katkılı zirkonya (%3 mol $Y_2O_3$ - %97 mol $ZrO_2$) tozları geleneksel seramik üretim yöntemi ile sentezlenmiştir. Karışımları aseton ortamda, mekanik alaşımlama yöntemiyle hazırladık. Mullit sentezi için stokiyometrik oranlarda hazırladığımız $Al_2O_3$ ve $SiO_2$ tozları karışımını hava ortamında 1600 $^oC$'de 3 saat fırınladık. İtriya katkılı zirkonya kompozitlerini ise, 1300 $^oC$'de 2 saat fırınladık. Böylece, itriya - zirkonya ve mullit kompozit fazları elde edildi ve öğütme ve eleme işlemleri yapıldı. Daha sonra mullit katkısız ve %10 mullit takviyeli itriyum oksit katkılı zirkonya karışımları toz metalurjisi yöntemiyle hazırlanmıştır. Kurutulduktan sonra, tozlar tek eksenli presleme ile sıkıştırılmıştır. Şekillendirilen numuneler, yüksek sıcaklıklı bir fırında hava koşullarında 1500 ve 1600 $^oC$ sıcaklıklarda, 1 ve 5 saat sürelerle sinterlenmiştir. Son olarak kompozitler üzerinde mikroyapı incelemeleri, faz analizi, 3 nokta eğilme, sertlik, aşınma testleri, su emme, gözeneklilik, büzülme ve yoğunluk sonuçları incelenmiştir. Sonuç olarak yapıdaki m-$ZrO_2$, t-$ZrO_2$ ve c-$ZrO_2$ miktarlarının sinterleme sıcaklığına ve süresine bağlı olarak değiştiğini anlıyoruz. Bu nedenle, tüm fiziksel ve mekanik özelliklerle birlikte, özellikle eğilme mukavemetleri değişmiştir. Ayrıca mullit ilavesi kompozitlerin eğilme mukavemeti, su emme ve gözeneklilik değerlerini artırırken; sertlik, aşınma, çekme ve yoğunluk değerlerini azalttığı sonucuna varılmıştır.

**Anahtar kelimeler:** Zirkonya, Mullit, İtriya, Karakterizasyon, Aşınma

## 1. Introduction

Among ceramics, zirconia ($ZrO_2$) and its composites have become very popular for technological and many scientific studies because of their good mechanical properties, corrosion resistance, low thermal conductivities, higher temperature stabilities and higher chemical stabilities [1-3]. They are preferred as important main materials for refractory materials, high temperature furnaces, components that are resistant to wear, various cutting tools, dental studies and other a lot of fields [1-4]. High-purity zirconia ($ZrO_2$) exhibits three polymorphs depending on temperature: monoclinic (m-$ZrO_2$) phase is stable at temperatures up to 1170 °C. After this temperature, the conversion from the monoclinic phase to the tetragonal phase begins and the tetragonal zirconia (t-$ZrO_2$) phase is stable up to 2370 °C temperatures. From this temperature to the melting temperature of 2680 °C, it is in the cubic zirconia phase (c-$ZrO_2$) [1,4]. Depend on the cooling processes, transformation from the t-$ZrO_2$ to m-$ZrO_2$ occurs. Transformation is very important because of resulting in a volumetric change of around 3% to 5% and so, leads to cracks. To prevent this transformation and stabilize the zirconia, it is common to use stabilizers. Addition of stabilizers to zirconia, lowers temperature of the transformations, reduces volumetric growth or shrinking and blocks the polymorphic transformations. With using stabilizers, it is possible to make stable the high-temperature phases at low temperatures too [4]. Different stabilizers, such as, $Al_2O_3$, CaO, $CeO_2$, MgO, $SiO_2$, $TiO_2$, $Y_2O_3$ and even a combination of them, stabilize and keep stable the zirconia in the t-$ZrO_2$ and/or c-$ZrO_2$ forms at low temperatures [5-7]. It is possible to produce materials consisting of only t-$ZrO_2$ or c-$ZrO_2$ or a mixture of these with m-$ZrO_2$ phases by adding different quantities of stabilizer. If less than sufficient stabilizing oxide is added, partially stabilized zirconia (PSZ) is obtained instead of fully stabilized zirconia. PSZ usually consists of two or more closely mixed phases. As a result of using stabilizers and obtaining fully or partially stabilized zirconia, could be achieved superb mechanical properties for example bending strength, hardness, fracture toughness [8].

Although, zirconia exhibits better mechanical properties than other ceramics, but like all other ceramics, it is fragile and cannot be formed at room temperature. So, we want to increase the toughness of these materials. For this, some energy absorbing mechanisms such as transformation toughening and fiber reinforcement are used in ceramic matrices [1].

In the method of increasing fracture toughness with transformation toughness, it works on the principle of a phase transformation caused by tension, by reducing the driving force that propagates existing cracks in the material structure [1]. The best example of this is zirconia. Zirconia which is added to the ceramic main phase, keeps important role in increasing fracture toughness and thus the bending strength with its tetragonal - monoclinic transformation toughening feature. With the discovery of the transformation toughening that occurs in zirconia, this material has found wide use. Because the main factor limiting the use of $ZrO_2$ in advanced engineering applications was the low toughness of this material. Increasing the toughness property with transformation toughness has also increased the interest in zirconia. The volume increase of 3 - 5%, which occurs with the tetragonal - monoclinic phase transformation in zirconia, prevents crack propagation, so increases the toughness of the material and its resistance to fracture [9]. The t-m transformation in zirconia can occur in different ways. For example: t-$ZrO_2$ can be free as a single particle or crystal; It can also be found in a compacted form in a matrix as a precipitate phase. Tetragonal zirconia particle size and the matrix in which the particles are compacted are the most important factors. A critical t-$ZrO_2$ grain size determine in $ZrO_2$. If the grain size is below this critical size, there will be no transformation; above, the t-m transformation occurs either continuously or as a result of applying a stress [10].

In the ceramic - ceramic mixed structure formation process, which is the other method of increasing the fracture toughness, the strength and toughness are increased by adding ceramic whiskers, fibers or particles to the main phase. This method is based on creating a physical barrier to the progressive crack. Having higher tensile strength than polycrystalline material, whiskers are a good barrier to propagation cracking. So, the fracture toughness of zirconium dioxide can be

increased more by adding some secondary phases for example nano particles, nano sized fibers or nano sheets into zirconia matrix [11]. For the last decades, improvement of nanomaterials offers new alternatives to reinforce ceramic composites. Carbon nanotubes have attracted important caution as reinforcement materials because of their magnificent properties. However, at high temperatures, they are prone to react with oxide matrixes leading to reduction in some mechanical properties of carbon nanotubes and limited the reinforcing effect on the composites [12,13]. So, it is stated that incorporation of mullite which is another type of ceramic toughening method with its high temperature oxidation and corrosion resistance and the other superior properties, might be preferred [11]. In the literature, mullite (3 $Al_2O_3$.2$SiO_2$) is described as the matchless stable middle crystalline phase for $Al_2O_3$-$SiO_2$ binary system, cost-friendly and exhibiting good refractory ability [14,15]. Mullite has received significant attention for technological applications because of its well properties like low coefficient of thermal expansion, high melting temperature, good resistance to creep, good chemical stability and satisfactory hardness [16,17]. In short, fracture toughness of zirconia can be advanced with mullite reinforcement as the secondary phase into the $ZrO_2$ matrix and so, the other mechanical properties can be improved too [11]. In addition, the temperature of sintering is also important, because of affecting some properties of ceramics through changing of the crystalline phases and microstructure [18].

In this study, we synthesized mullite (3$Al_2O_3$.2$SiO_2$) and 3 mol % yttrium oxide doped zirconium dioxide powders by conventional ceramic production method. We examined whether there are phase differences in the $Y_2O_3$-$ZrO_2$ mixture depend on sintering temperatures and times and the effect of mullite on the physical, mechanical and microstructural properties of these mixtures.

## 2. Materials and Methods

Mullite and yttria doped zirconia powders were produced by conventional ceramic production method in this study. All precursory powder materials ($Al_2O_3$, $SiO_2$, $Y_2O_3$ and $ZrO_2$) were obtained from Company Eczacıbası, Alfa Aesar and Chemicals of Handan Yaxiang Trading Co., Ltd (Eczacıbası Esan, Turkey; Alfa Aesar, United States of America and Handan Yaxiang Chemicals Trading Co., Ltd, China). The powders were mixed in acetone environment by mechanical alloying method. The powders were heated for 24 hours in oven at 110 ºC before and after mixing. Mullite (3$Al_2O_3$.2$SiO_2$) and 3 mol% yttria doped zirconia ($Y_2O_3$-$ZrO_2$) powders were synthetized by sintering from the prepared powders with stoichiometric ratios of $Al_2O_3$, $SiO_2$, $Y_2O_3$ and $ZrO_2$ powders after homogenized in ball mill. Mullite (3$Al_2O_3$.2$SiO_2$) was synthetized for 3h at 1600 ºC and 3 mol% yttria doped zirconia ($Y_2O_3$-$ZrO_2$) composite powders were synthetized for 2 h at 1300 ºC. Thus, yttria - zirconia and mullite composite phases were obtained and grinding and sieving processes were carried out. Then, we prepared mullite-free and 10% by weight mullite reinforced cerium oxide added zirconium oxide composites with powder metallurgy technique (these mixtures were coded as YZ0M and YZ10M). The sample was coded as YZ10M16005 (YZ: Yttria doped zirconia; 10M: 10% Mullite addition and 16005: 1600 °C sintering temperature and 5 hours sintering time). After the composite powders were milled for 24 h in acetone environment with zirconia ball mill, sieved and dried. Then, the composite mixtures were pressed to 56x12 mm sizes mold gap by uniaxial pressing machine at 200 MPa load. The pressed samples were sintered in a high temperature owen (Protherm) and in air conditions for 1-5 h sintering times and 1500-1600 ºC temperatures. The heating rate was 5 ºC/min. Then, with SEM, microstructure investigations, phase analysis with XRD, 3-point bending, hardness and wear tests, absorption of water, porosity, shrinkage and density results were examined on the composites.

The three-point flexural strength tests were executed with 0.5 mm/min (crosshead speed) in a Shimadzu brand tensile-compression device. For each sample, measurements were taken five times and their average were taken as the bending strength results of the samples. The strength calculations were made with the formula (1):

$$\sigma = 3/2*P*L / (b*h^2) \quad (1)$$

(In (1) the letters mean that, P: maximum force, L: the distance of between supports, b: width of samples, h: height of samples).

After 180, 320, 600, 1200 and 2500 grit sanding process, polishing is done for each sample. With Vickers hardness tester that was Mitutoyo brand, the measurements of hardness were executed by 1 kg load for 10 seconds. For each sample, measurements were taken five times and their average were taken as the hardness results of the samples [19-24]. The wear tests of samples were executed with Plint brand wear tester. For wear tests, steel discs were used. For each sample, wear tests were executed at 400 rpm rate, 5, 10 and 15 min wear durations and 100 N force. The samples were weighted with a precision scale of $10^{-4}$ g. After the assigned wear times, the samples were scaled again and the wear amounts were calculated [22,23]. To determine the phases, XRD with Cu Kα radiation (Bruker AXS D8 Advance; 20kV-60kV, 6mA-80mA and θ = 10º-90º, 0.002º) was used. The phases of the samples seen in XRD patterns were defined with the Panalytical X'Pert program. The microstructural characterization of the samples was made with the Mira3XMU FE-SEM (Tescan, Czech Republic) brand SEM (scanning electron microscope) machine with EDS (energy dispersion spectrum). The results were presented in various graphics and tables and some comments on these results were made.

## 3. Results and Discussions

Physical (shrinkage, water absorption, density and porosity tests) and mechanical (wear, 3-point bending and hardness) tests, SEM, EDS and XRD analysis results were included in this section. Calculations and measurements were repeated 5 times and arithmetic averages were taken.

The shrinkage, porosity, water absorption, relative density and bulk density results are shown in Table 1, and also Fig. 1. In Fig. 1, the relative density values were taken at the rate of 1/3 of the actual values for the graph to be more understandable.

**Table 1.** Physical test results of YZ0M and YZ10M samples.

| Samples | Bulk density g/cm$^3$ | Relative density (%) | Water Absorption (%) | Porosity (%) | Shrinkage (%) |
|---|---|---|---|---|---|
| YZ00M15001 | 5,06 | 89,47 | 2,09 | 10,53 | 12,64 |
| YZ00M15005 | 5,48 | 96,80 | 0,22 | 3,20 | 14,71 |
| YZ00M16001 | 5,56 | 98,31 | 0,19 | 1,69 | 15,28 |
| YZ00M16005 | 5,57 | 98,44 | 0,18 | 1,56 | 15,50 |
| YZ10M15001 | 4,66 | 87,59 | 2,02 | 12,41 | 11,38 |
| YZ10M15005 | 4,90 | 92,13 | 0,41 | 7,87 | 12,75 |
| YZ10M16001 | 5,12 | 96,15 | 0,14 | 3,85 | 13,64 |
| YZ10M16005 | 5,03 | 94,60 | 0,18 | 5,40 | 13,50 |

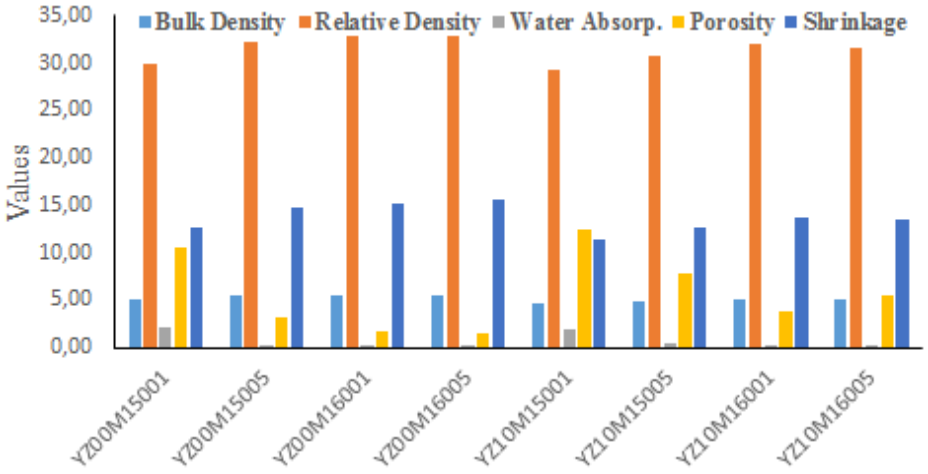


**Figure 1.** Physical test results graph of YZ0M and YZ10M samples.

When the results were examined, it was found that with increasing sintering temperature and time, the shrinkage values increased in general. We know that when the shrinkage values are higher, the water absorption and porosity values decrease and our results confirm this. And so, it is seen that experimental density and relative density values increase.

Due to the lower density of mullite compared to the $ZrO_2$-$Y_2O_3$ composite, the mullite-added samples have lower density and shrinkage values and contrary to this, higher porosity and water absorption. We think that the decrease in the density value of the mullite-added 16005 sample is caused by defects such as excessive grain growth and formation of large pores in the microstructure depending on the sintering time.

Table 2, Figure 2 and Figure 3 indicated hardness and three-point flexural strength results of YZ0M and YZ10M samples.

**Table 2.** Hardness and three-point flexural strength results of YZ0M and YZ10M samples.

| Samples | Hardness (HV) | 3 Point Bending Strength (MPa) |
|---|---|---|
| YZ00M15001 | 526,35 | 82,71 |
| YZ00M15005 | 767,33 | 110,99 |
| YZ00M16001 | 928,85 | 189,88 |
| YZ00M16005 | 920,13 | 111,15 |
| YZ10M15001 | 512,00 | 77,31 |
| YZ10M15005 | 673,83 | 142,23 |
| YZ10M16001 | 840,87 | 176,19 |
| YZ10M16005 | 792,95 | 251,63 |

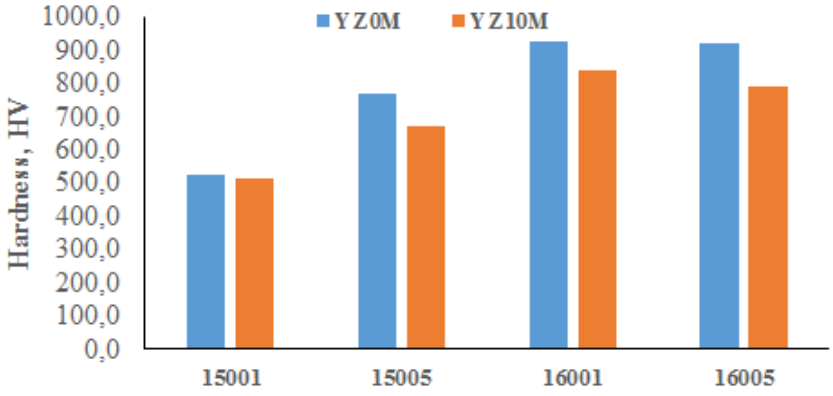


**Figure 2.** Hardness graph of samples.

When the hardness test results are examined, with increasing sintering temperature and time, we see the hardness values generally rise related to the shrinkage, porosity and density values. Because of higher porosity, hardness values of mullite-added samples are lower than mullite-free samples similar to density results. It is seen that hardness values of 16005 specimens with and without mullite additives decreased. The decrease in hardness values of 16005 samples is a result of large pores formed in the microstructure and possible phase changes.

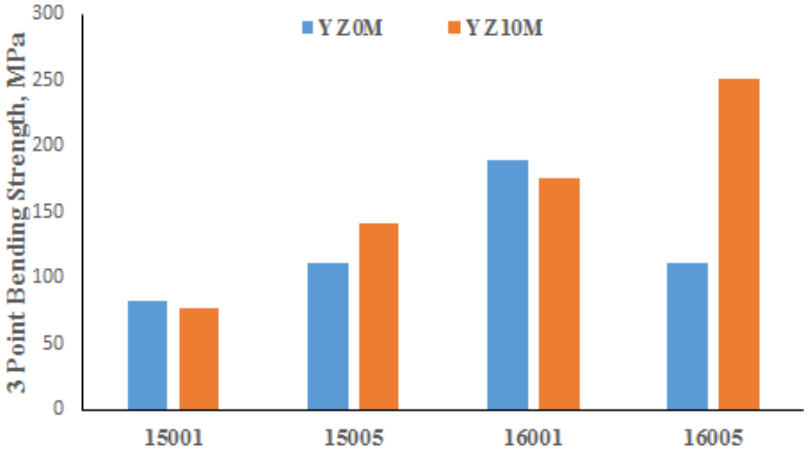


**Figure 3.** 3-Point bending strength graph of samples.

According to the results, it is seen that the three-point bending strength values generally increase with higher sintering temperature and time, and the highest value is obtained in the mullite-added 16005 sample. We think that the decrease in the three-point bending strength of the mullite-free sample 16005 is due to possible phase changes in the structure.

Considering that the flexural strength results change significantly with the amount of tetragonal phase in the structure, this situation is thought to be a result of the effect of the sintering temperature and time on the phases in the structure, as stated in the XRD analysis section. However, this is not exactly the case in mullite-added samples. Although lower amount of tetragonal $ZrO_2$ phase, bending strength values of the mullite-added samples for 15005 and 16005 specimens are higher. This shows that the mullite additive acts as toughening and increases the flexural strength of these samples.

The wear tests of samples were executed with Plint brand wear tester. For wear tests, steel discs were used. For each sample, wear tests were executed at 400 rpm rate, 5, 10 and 15 min wear durations and 100 N force. The samples were weighed with a precision scale of $10^{-4}$ g. After the assigned wear times, the samples were scaled again and the wear amounts were calculated. Wear results are seen in Table 3 and Fig. 4.

**Table 3.** Wear results of YZ0M and YZ10M samples.

| Samples | Wear Volume ($mm^3$), 100 N | | |
|---|---|---|---|
| | 5 min. | 10 min. | 15 min. |
| YZ00M15001 | 0,161 | 0,288 | 0,511 |
| YZ00M15005 | 0,110 | 0,183 | 0,329 |
| YZ00M16001 | 0,072 | 0,114 | 0,203 |
| YZ00M16005 | 0,090 | 0,126 | 0,216 |
| YZ10M15001 | 0,214 | 0,377 | 0,715 |
| YZ10M15005 | 0,162 | 0,273 | 0,596 |
| YZ10M16001 | 0,124 | 0,215 | 0,352 |
| YZ10M16005 | 0,098 | 0,178 | 0,295 |

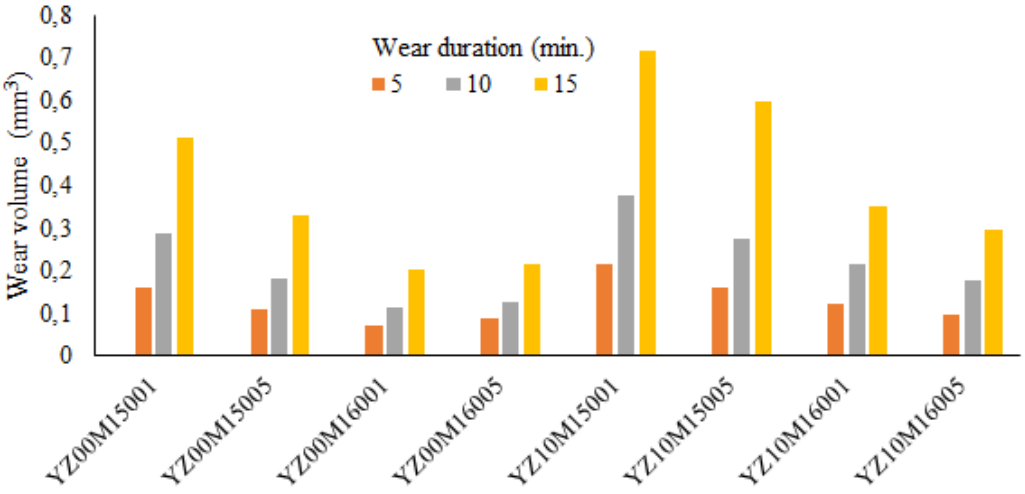


**Figure 4.** Wear test results graph of samples.

When the data obtained are examined, it is seen that the wear results vary depending on the hardness, bending strength and wear time of the samples. In general, as the wear time increased, the amount of wear of the samples also increased. It is understood that the wear resistance of the samples with high hardness and bending strength is better. Because of the lower hardness and higher porosity, mullite additive affected these samples negatively and decreased the wear resistance a little bit. Although the hardness value of the mullite-added 16005 sample decreased, the wear resistance was good, indicating that besides the hardness values, the flexural strengths of these samples have a significant impact on the wear properties too. Adhesive type wear was observed in these samples.

The phase changes in the sample structure related with the temperature and time of YZ0M and YZ10M samples were analyzed and the basic phases that emerged in the structure were shown in Figure 5 and Figure 6.

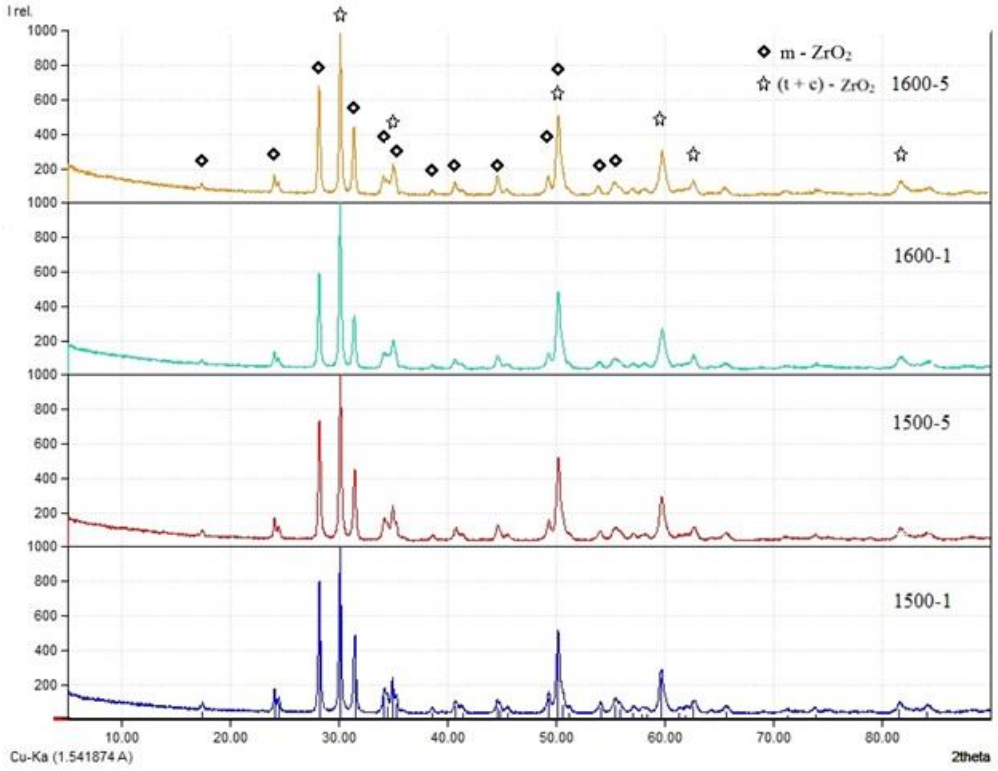

**Figure 5.** XRD patterns of YZ0M samples.

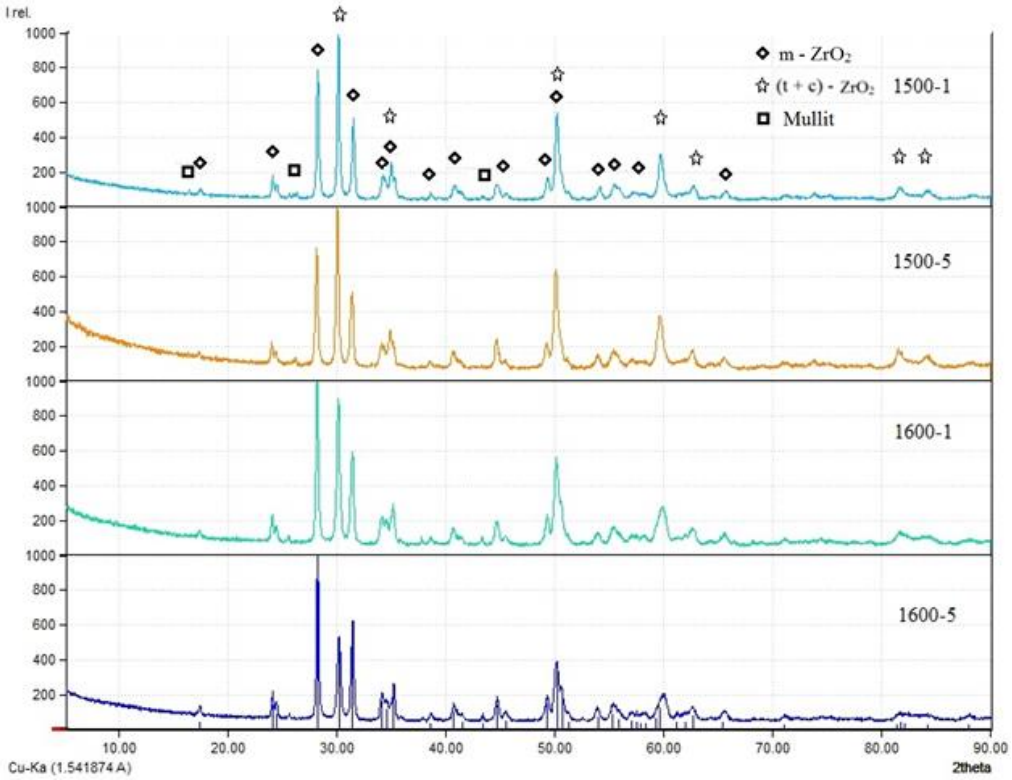


**Figure 6.** XRD patterns of YZ10M samples.

Stawarczyk et al [25] produced $Y_2O_3$ - $ZrO_2$ composite ceramics by sintering for 2 hours at temperatures between 1350 $^oC$ and 1700 $^oC$. They stated that above 1600 $^oC$, grain growth and voids occurred and the highest bending strength was obtained between 1400 $^oC$ and 1550 $^oC$ temperatures.

Çevlik [26], in his thesis study, gives the information that the superior mechanical properties are largely dependent on the critical grain size. This is stated that above the critical grain size, the tetragonal $ZrO_2$ phase spontaneously transforms into the monoclinic $ZrO_2$ phase, reducing the fracture toughness and bending strength.

The highest m-$ZrO_2$ phase ratio is seen in the 15001 sample in the XRD patterns of the mullite-free samples given in figure 5. Therefore, the bending strength value was also the lowest in this sample. The highest flexural strength value belongs to the 16001 sample with the lowest monoclinic phase. As the monoclinic $ZrO_2$ phase ratio increased again in the 16005 sample, the bending strength decreased.

In the XRD figures of the mullite added samples given in Figure 6, it is seen that the tetragonal and cubic $ZrO_2$ phases decrease, while the m-$ZrO_2$ phase increases with rising sintering temperature and time. Although the m-$ZrO_2$ phase increasing, the increase in the bending strength of the specimens is explained with the study of Huang et al [27]. In this study, it was stated that as a result of the homogeneous distribution of the $ZrO_2$ particles in the mullite, some mechanical properties of the mullite improve and thus the composite structure is strengthened. In addition, the alumina particles that do not react and remain in the structure are evenly distributed in the structure and advance the mechanical properties of the sample. They stated that the mullite formed as a result of the reaction was distributed in the $ZrO_2$ matrix and the mullite amount and size raised with the increasing the sintering temperature.

In this direction, although the most prominent feature for flexural strength in mullite-free samples is the high amount of tetragonal $ZrO_2$ in the structure, and therefore due to t-m transformation

toughening; It is understood that this situation is not valid alone in mullite added samples. The flexural strength of these samples varies mostly depending on the state of the mullite in the structure. In addition, in the mentioned study, it was stated that residual alumina and $SiO_2$ appeared in the structure of the mullite-doped specimens, and the secondary phase toughening mechanism increased the bending strength with the effect of these particles. It was also stated that Si and Al elements occur outside the mullite region and do not completely react while forming mullite. However, it was noted that a small quantity of residual Si element can be found in the zirconia matrix. Additionally, we think that the decrease in the density value in mullite added 16005 samples may be due to the swelling effect as a result of the growth of mullite grains and the increase in the amount of m-$ZrO_2$ phase in the structure.

Liu et al [28] stated in their study that by adding mullite to 3Y-TZP, the bending strength values increased with the addition of mullite, although the hardness values decreased. This toughening effect of mullite is explained by Liu et al as follows: Even if the crack emerging in the structure passes by breaking apart a mullite grain, its energy will decrease, and when it coincides with the next mullite grains, the energy will decrease and the crack will change direction. Again, by being blocked by secondary phase particles such as residual alumina in the structure, the crack will change direction again, lose its energy and stop its progress by damping [28].

The SEM images and EDS analyzes of YZ00M16005 and YZM10M16005 samples are given in Figure 7 and Figure 8.

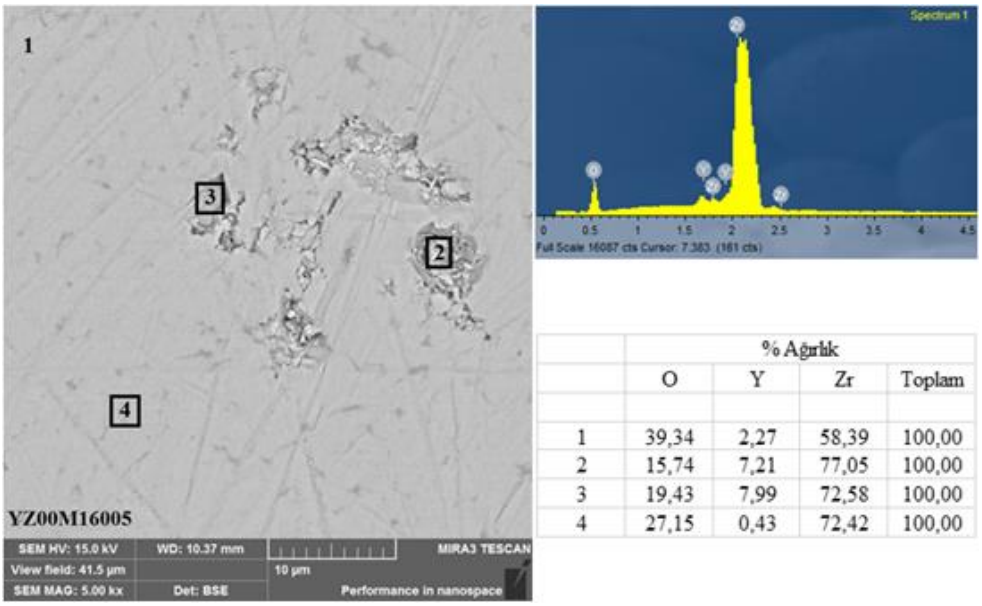


| | % Ağırlık | | | |
|---|---|---|---|---|
| | O | Y | Zr | Toplam |
| 1 | 39,34 | 2,27 | 58,39 | 100,00 |
| 2 | 15,74 | 7,21 | 77,05 | 100,00 |
| 3 | 19,43 | 7,99 | 72,58 | 100,00 |
| 4 | 27,15 | 0,43 | 72,42 | 100,00 |

**Figure 7.** SEM image and EDS analyses of YZ00M16005 sample.

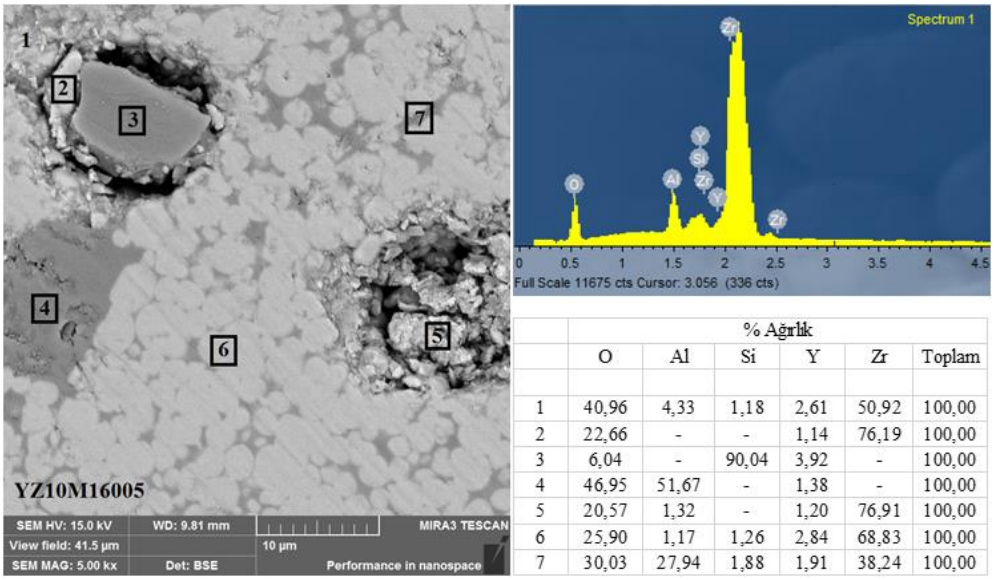


| | % Ağrlık | | | | | |
|---|---|---|---|---|---|---|
| | O | Al | Si | Y | Zr | Toplam |
| 1 | 40,96 | 4,33 | 1,18 | 2,61 | 50,92 | 100,00 |
| 2 | 22,66 | - | - | 1,14 | 76,19 | 100,00 |
| 3 | 6,04 | - | 90,04 | 3,92 | - | 100,00 |
| 4 | 46,95 | 51,67 | - | 1,38 | - | 100,00 |
| 5 | 20,57 | 1,32 | - | 1,20 | 76,91 | 100,00 |
| 6 | 25,90 | 1,17 | 1,26 | 2,84 | 68,83 | 100,00 |
| 7 | 30,03 | 27,94 | 1,88 | 1,91 | 38,24 | 100,00 |

**Figure 8.** SEM image and EDS analyses of YZ10M16005 sample.

From the SEM images of the specimens given in Figure 7 and Figure 8, it is understood that the grain size and distribution are generally homogeneous in the mullite added sample, but some different particles on the surface form pores and disrupt the homogeneous structure. It can be predicted that this situation will have a negative effect on the hardness values of the specimens and decrease the hardness value of the mullite added sample. As a matter of fact, in the experimental results, the hardness value of the YZ10M16005 sample was found to be lower than the hardness value of the YZ00M16005 sample.

According to the EDS analyzes given in Figure 7 and Figure 8, the evaluation of the EDS results for the YZ00M16005 and YZ10M16005 samples was made from general (1) and parts 2, 3, 4, 5, 6, 7. It has been observed that the results of the EDS elemental analysis made from the general field survey (1) and other parts are compatible with the contribution rates and XRD results made to the samples.

## 4. Conclusions

In YZ0M coded samples, with increasing sintering temperature and time, generally shrinkage, experimental density, relative density, hardness and three-point bending strength values and wear resistance increased; It was observed that the water absorption and porosity values decreased. Among these samples, the three-point flexural strength and hardness values of the 16005 sample and the wear resistance decreased. The highest m-$ZrO_2$ phase ratio was found in sample 15001 in mullite-free samples. Therefore, the bending strength value is also the lowest in this sample. The highest flexural strength value belongs to the 16001 sample with the lowest m-$ZrO_2$ phase. As the m-$ZrO_2$ phase ratio increased in the 16005 sample, the flexural strength and hardness decreased.

In YZ10M coded mullite added samples, with increasing sintering temperature and time, generally shrinkage, experimental density, relative density, hardness and three-point bending strength values and wear resistance increased; It was observed that the water absorption and porosity values decreased. A decrease was observed in the density and hardness values of the mullite added 16005 sample. It was determined that t-$ZrO_2$ and c-$ZrO_2$ phases decreased, m-$ZrO_2$ phase increased and 16005 sample had the highest m-$ZrO_2$ phase with increasing the sintering temperature and time in mullite added YZ10M samples. So, we think that the decrease in the density value in mullite-doped 16005 samples may be related with the increase in the amount of m-$ZrO_2$ phase in the structure and the swelling effect as a result of the growth of mullite grains. The mullite additive reduced the

shrinkage, experimental density, relative density, hardness values and wear resistance of the samples. But It was observed that the water absorption, porosity and three-point flexural strength values increased in general and the highest flexural strength value was obtained in the 16005 specimen with mullite additive. This shows that the mullite additive acts as toughening and increases the flexural strength of these samples. Despite the decrease in hardness value of the mullite-added 16005 sample, the good wear resistance shows that the bending or flexural strength of these specimens has an effect on the wear properties.

While m-$ZrO_2$, t-$ZrO_2$ and c-$ZrO_2$ phases were detected in mullite-free samples; It was determined that in addition to these phases, mullite phase was also present in the mullite added samples.

This study proves that, mullite additive can be used to increase the bending strength of the $ZrO_2$-$Y_2O_3$ ceramic composites. Although lower hardness results with adding mullite reinforcement, good wear properties can be obtained from higher bending strength with mullite additive. In addition, it is understood that lighter and stronger composites can be obtained with mullite additive.

**Conflict of Interest:** No conflict of interest was declared by the authors. This paper has been presented at the ICENTE'21 (International Conference on Engineering Technologies) held in Konya (Turkey), November 18-20, 2021.

**Financial Disclosure:** This work is supported by the Scientific Research Project Fund of Sivas Cumhuriyet University under the project number M-767. Authors would like to acknowledge Scientific Research Project Fund of Sivas Cumhuriyet University.

**References**

[1] Boyraz, T., 2008. “An investigation on physical and electrical properties of CaO/MgO-stabilized zirconia ceramics formed with different methods,” Ph.D. dissertation, Metallurg. Eng., Istanbul Technical Univ., Istanbul.

[2] Pekdemir, A. D., 2018. “Preparation and characterization of boron carbide at low-temperature from boric acid and polyols,” Ph.D. dissertation, Dept. Chem., Ankara Univ., Ankara.

[3] Ceylan, A., 2006. “The production of functionally graded SiAlON ceramics by tape casting method,” Ph.D. dissertation, Dept. Cer. Eng., Anadolu Univ., Eskişehir.

[4] Abi, C. B., 2009. “An investigation on fracture toughness of traditional and technical ceramics,” Ph.D. dissertation, Dept. Metallurg. Eng., Afyon Kocatepe Univ., Afyon.

[5] Hafızoğlu, M. A., Boyraz , T. and Akkuş, A., 2021. “Fabrication, characterization and wear properties of mullite reinforced silica-doped zirconia ceramic composites,” in Proc. IMSMATEC'21, p. 175 – 180.

[6] Hafızoğlu, M. A., Akkuş, A. and Boyraz, T., 2021. “Fabrication, characterization and wear properties of mullite reinforced Al2O3-doped ZrO2 ceramic composites,” in Proc. GLOBCER’21, p. 673 – 686.

[7] Hafızoğlu, M. A., Boyraz , T. and Akkuş, A., 2021. “Fabrication and characterization of mullite reinforced TiO2 added ZrO2 ceramics,” International Joint Science Congress of Materials and Polymers (ISCMP’21).

[8] Cutler, R. A., Reynolds, J. R. and Jones, A., 1992. “Sintering and characterization of polycrystalline monoclinic, tetragonal, and cubic zirconia,” Journal of the American Ceramic Society, 75(8), pp. 2173-2183.

[9] Boyacıoğlu, T., 2007. “Improvement of room temperature mechanical properties of various amount of metal oxide doping cubic zirconia (c-ZrO2) used as electrolyte material for solid oxide fuel cells,” Master thesis, Dept. Metallurg. Eng., Gazi Univ., Ankara.

[10] Boyraz, T., 1998. “Dental porcelain powders,” Master thesis, Dept. Metallurg. Eng., Sakarya Univ., Sakarya.

[11] Liu, P. F., Li, Z., Xiao, P., Luo, H. and Jiang, T. H., 2018. "Microstructure and mechanical properties of in-situ grown mullite toughened 3Y-TZP zirconia ceramics fabricated by gelcasting," Ceramics International, 44(2), pp. 1394-1403.

[12] Eichler, J., Rödel, J., Eisele, U. and Hoffman, M., 2007. "Effect of grain size on mechanical properties of submicrometer 3Y-TZP: fracture strength and hydrothermal degradation," Journal of the American Ceramic Society, 90(9), pp. 2830-2836.

[13] Sun, J., Gao, L., Iwasa, M., Nakayama, T. and Niihara, K., 2005. "Failure investigation of carbon nanotube/3Y-TZP nanocomposites," Ceramics International, 31(8), pp. 1131-1134.

[14] El Ouatib, R., Guillemet, S., Durand, B., Samdi, A., Rakho, L. E. and Moussa, R., 2005. "Reactivity of aluminum sulfate and silica in molten alkali-metal sulfates in order to prepare mullite," Journal of the European Ceramic Society, 25(1), pp. 73-80.

[15] Kucuk, I. and Boyraz, T., 2019. "Structural and mechanical characterization of mullite and aluminium titanate reinforced yttria stabilized zirconia ceramic composites," Journal of Ceramic Processing Research, 20(1), pp. 73-79.

[16] Kumar, P., Nath, M., Ghosh, A. and Tripathi, H. S., 2015. "Enhancement of thermal shock resistance of reaction sintered mullite–zirconia composites in the presence of lanthanum oxide," Materials Characterization, 101, pp. 34-39.

[17] Roy, J., Das, S. and Maitra, S., 2015. "Solgel-processed mullite coating—a review. International Journal of Applied Ceramic Technology, 12, pp. E71-E77.

[18] Denry, I. and Kelly, J. R., 2008. "State of the art of zirconia for dental applications," Dental materials, 24(3), pp. 299-307.

[19] Çitak, E. and Boyraz, T., 2014. "Microstructural characterization and thermal properties of aluminium titanate/YSZ Ceramics," Acta Physica Polonica A, 125(2), pp. 465-468.

[20] Önen, U. and Boyraz, T., 2014. "Microstructural characterization and thermal properties of aluminium titanate/spinel ceramic matrix composites," Acta Phys. Pol. A, 125(2), pp. 488-490.

[21] Sacli, M., Onen, U. and Boyraz, T., 2015. "Microstructural characterization and thermal properties of aluminium titanate/porcelain ceramic matrix composites," Acta Physica Polonica A, 127(4), pp. 1133-1135.

[22] Boyraz, T. and Akkuş, A., 2021. "Investigation of wear properties of mullite and aluminium titanate added porcelain ceramics," Journal of Ceramic Processing Research. Vol. 22, No. 2, pp. 226-231.

[23] Akkus, A. and Boyraz, T., 2018. "Investigation of wear properties of CaO, MgO added stabilized zirconia ceramics produced by different pressing methods," J. Ceram. Proc. Res., Vol. 19, pp. 249-252.

[24] Kucuk, I., Boyraz, T., Gökçe, H. and Öveçoğlu, M. L., 2018. "Thermomechanical properties of aluminium titanate (Al2TiO5)-reinforced forsterite (Mg2SiO4) ceramic composites," Ceramics International, 44(7), pp. 8277-8282.

[25] Stawarczyk, B., Özcan, M., Hallmann, L., Ender, A., Mehl, A. and Hämmerlet, C. H., 2013. "The effect of zirconia sintering temperature on flexural strength, grain size, and contrast ratio," Clinical oral investigations, 17(1), 269-274.

[26] Talay Çevlik, E., 2015. "Low thermal degradation of three yttria-stabilized tetragonal zirconia polycrystalline and effect of low thermal degradation on flexural strength," Ph.D. dissertation, Dept. Dent., Selçuk Univ., Konya.

[27] Huang, Y. Q., Liu, P. F., Li, Z. and Xiao, P., 2018. "Effects of the content of insitu grown

mullite on the microstructure and mechanical properties of 3Y-TZP ceramics fabricated by gel-casting," Ceramics International, 44(17), pp. 21882- 21892.

[28] Liu, P. F., Li, Z., Xiao, P., Luo, H. and Jiang, T. H., 2018. "Microstructure and mechanical properties of in-situ grown mullite toughened 3Y-TZP zirconia ceramics fabricated by gelcasting," Ceramics International, 44(2), pp. 1394-1403.

OPEN JOURNAL OF NANO

# Laser Surface Texturing and Techniques to Improve the Tribological Properties of Materials

[1]Setenay Gemici, [1]Yaşar Demircan, *[1]Abdullah Sert

[1]Eskişehir Osmangazi University, Faculty of Engineering and Architecture, Department of Mechanical Engineering, 26040, Eskişehir
* Corresponding author, e-mail: asert@ogu.edu.tr,

Submission Date: 23.10.2021 Acceptation Date: 25.12.2021

**Abstract** - Surface texturing, a technological method in the last decade, is one of the surface modification techniques that change the surface texture to improve the tribological properties of materials. It provides an increase in the wear resistance of the materials and a decrease in the friction coefficients, as well as improving the lubrication conditions. Recently, various surface texturing processes have been developed. One of them, laser surface texturing, is the most advanced and efficient among them. Different texture density, size, depth and shape changes on the surfaces of materials with laser surface texturing have been the subject of theoretical and experimental researches. In this review study, laser ablation, laser interference and laser shock, which are the most commonly used techniques, were examined in detail from the literature and compiled within the scope of this study. In laser surface modification methods, the parameters affecting tribological properties such as texture geometry and laser power, laser pulse and laser scanning speed are discussed. The tribological behaviors of laser texturing under different operating conditions (dry and oily) were also investigated.

**Keywords:** Coefficient of Friction, Laser Ablation, Laser Interference, Laser Shock Processing, Laser Surface Texturing

# Malzemelerin Tribolojik Özelliklerini İyileştirmeye Yönelik Lazer Yüzey Tekstür ve Teknikleri

**Öz** - Son on yılda teknolojik bir yöntem olan yüzey tekstür yöntemi, malzemelerin tribolojik özelliklerini geliştirmek için kullanılan yüzey modifikasyon tekniklerinden biridir. Malzemelerin aşınma direncinin artmasını ve sürtünme katsayılarının azalmasını sağlar ve bunun yanı sıra yağlama koşulları iyileştirir. Son zamanlarda çeşitli yüzey tekstüre işlemleri geliştirilmiştir. Bunlardan biri olan lazer yüzey tekstüre işlemi aralarındaki en gelişmiş ve verimli olanıdır. Lazer yüzey tekstüre ile malzemelerin yüzeylerinde farklı doku yoğunluğu, boyut ve derinlik ve şekil değişiklikleri teorik ve deneysel araştırmalara konu olmuştur. Bu derleme çalışmasında, en yaygın kullanılan teknikler olan lazer ablasyonu, lazer girişimi ve lazer şoku literatürdeki kaynaklardan detaylı olarak incelenmiş ve bu çalışma kapsamında derlenmiştir. Lazer ile yüzey modifikasyonu yöntemlerinde tribolojik özellikleri etkileyen parametrelerden tekstür geometrisi ile lazer gücü, lazer şoklama ve lazer tarama hızı gibi konular ele alınmıştır. Farklı çalışma koşulları altında (kuru ve yağlı), lazer tekstür işleminin tribolojik davranışları da ayrıca incelenmiştir.

**Keywords:** Sürtünme Katsayısı, Lazer Ablasyon, Lazer İnterferans, Lazer Şok İşleme, Lazer Yüzey Tekstüre

[1] Corresponding author: Tel: (0222) 239 37 50
E-mail: asert@ogu.edu.tr

## 1. Introduction

Surface modification methods have been preferred for years in order to improve tribological properties. These methods are laser surface texturing (LST) [1-4], ion beam etching/milling [5-7], lithography [8-11], hot embossing [12-14], micro-milling [15-18], electrochemical machining [19-20], and mechanical texturing [21].

Extending the lifetime of engineering materials can be provided with LST, a technology that optimizes micro topography [22]. LST is preferred among surface texturing methods due to its high efficiency, excellent controllability, environmental friendliness and accuracy [23]. In severe sliding conditions on the material, laser texturing is known to increase load bearing capacity and reduce friction [22]. Various laser methods are used in the literature to create textures on the surface of engineering materials. Direct laser ablation [23], direct laser interference [24] and laser shock processing [25] are the main methods used in LST. Comparison of LST techniques were given in Table 1.

Table 1. Comparison of LST techniques [27].

| Criteria | Laser interference | Laser ablation | Laser shock processing |
|---|---|---|---|
| **Efficiency** | xxxx | xxxx | xxx |
| **Flexibility** | xxxxx | xxx | xxx |
| **Surface modification effect mechanism** | Heat induced phase transformation | Heat induced phase transformation | Surface plastic deformation for all metallic materials |
| **Resolution** | 0.1 µm for silicon substrate | 1 µm for titanium | 10 µm for aluminum alloy |
| **Applicable materials** | Metals, polymer, ceramics and composite materials | Metals, polymer, ceramics and composite materials | Metals |

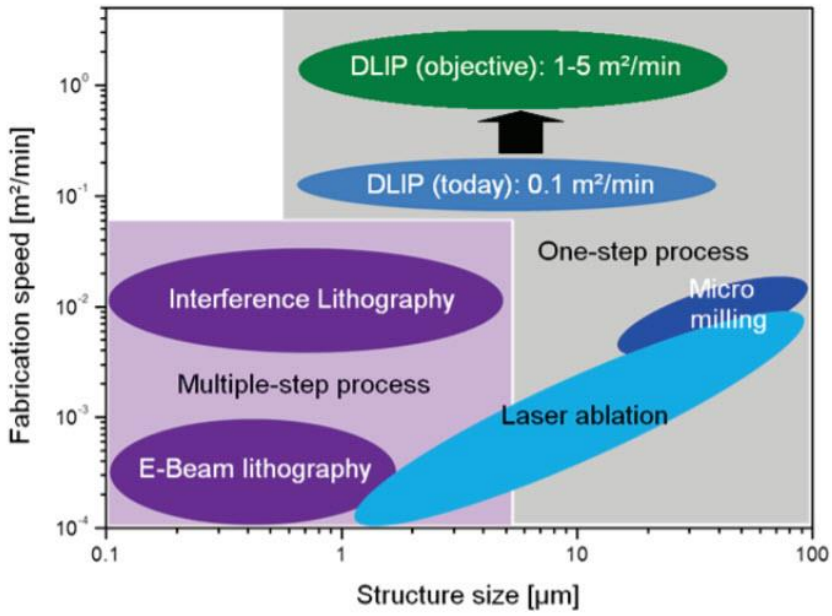


Figure 1. A comparison of different surface texturing techniques in terms of structure size and fabrication speed [26]

As can be seen in the Figure 1, the production speed can be 0.1 $m^2$/min with a structure size ranging from 1 to 100 µm with the laser interference technique. With this feature, it is more efficient than lithography and laser ablation techniques. Compared to the laser ablation method, the interference technique is more advantageous in terms of resolution [26].

The LST process is used to improve lubrication and increase wear behavior. With the LST technique, the decrease in the contact area between the surfaces of the materials and the increase in the surface hardness during the process increase the wear resistance of the materials [27]. In addition, the particles that worn off from the surfaces in contact trapped by the textures opened with LST, preventing the acceleration of wear [28]. The friction coefficient decreases with the decrease of the actual contact area of the surfaces in contact and the formation of the surface hardening mechanism with LST technique [29].

Micro dimples produced with LST can serve as a micro reservoir for lubricant in starved lubrication conditions and as a micro hydrodynamic bearing in full or mixed lubrication conditions [28].

Analysis of tribological parameters of engineering materials processed with LST is important for overall improvement of the process and emerging commercial applications. LST is used in biomedical applications [23] to improve the biocompatibility of ceramic implant prostheses [29] and in the automotive industry [30] to improve paint adhesion on surfaces. Tribological applications such as mechanical seals, piston rings, thrust bearings and cylinder liner segments [31] have been developed for the latest status of LST and the potential of this technology [32]. LST is used to improve surface tribology parameters on polymer surfaces such as polypropylene copolymer [30] and Polytetrafluoroethylene (PTFE) [33], ceramics [34], Ti-6Al-4V alloy (TC4) substrate surface [35].

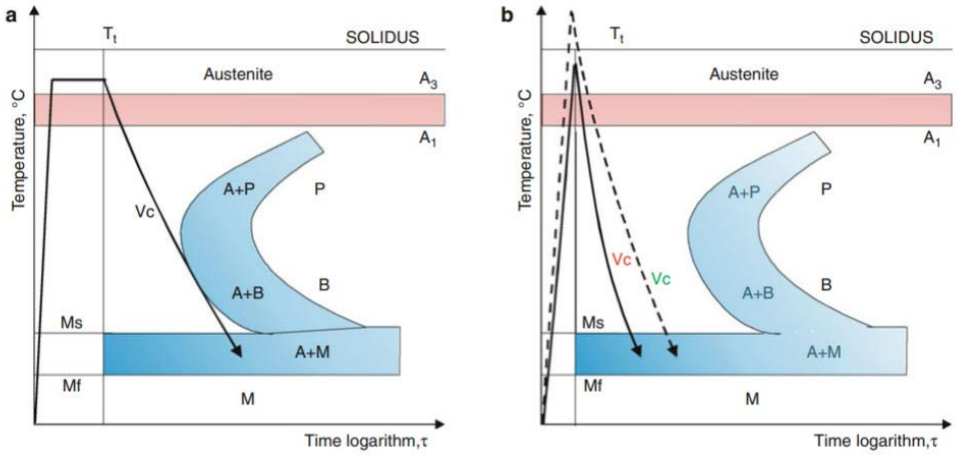


Figure 2. Schematic of hardening using (a) conventional treatment, (b) laser treatment; heat treatment [36]

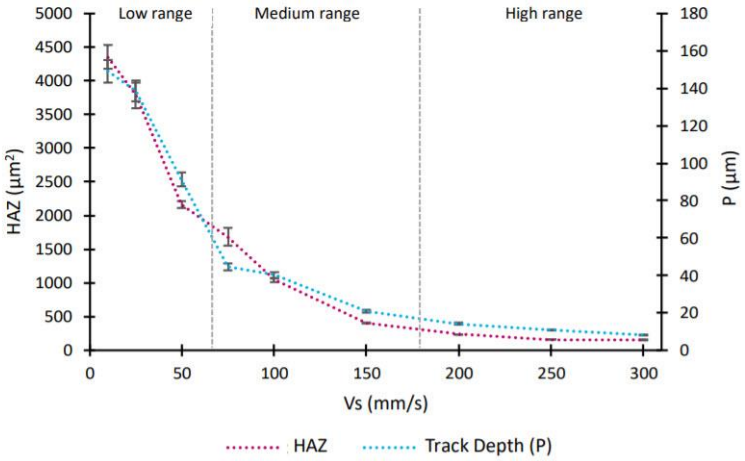


Figure 3. Heat-affected zone (HAZ) and depth of laser tracks as a function of Vs [37]

In terms of laser surface treatment, thermal effects on the material differ from other method. Figure 2 shows the schematic Time- Temperature-Transform (TTT) diagram of conventional and laser heat treatments. As it can be seen from the curves on the figure, since the laser process will be faster than the conventional process, rapid heating and cooling occurs in the microstructure. Especially in heat treatments with laser, the cooling rate is high because the area affected by the laser is quite small. Therefore, the microstructure formed after heat treatment is finer than conventional heat treatment. The thermal effect of the laser process, especially on the material, is also related to the speed of the process. In a study [37], the width of the heat affected zone (HAZ) is given in Figure 3, depending on the scanning speed of the laser process. It is seen that the HAZ decreases with the increase of scanning speed.

In this study, the effects of the worldwide existing technology related to LST on tribological applications are examined in detail from the literature and their analyzes are given. Process designs of major methods of LST techniques are reviewed and compared.

## 2. Laser Surface Texture Techniques (Process Design)

Studies show that there are various methods for creating textures or patterns produced on engineering materials. Among the LST techniques, commonly used three methods are: LST by Direct Laser Ablation, LST by Direct Laser interference Patterning (DLIP), and LST by Laser Shock Processing (LSP). This chapter provides a detailed review of laser surface patterning using these methods.

### 2.1. LST By Direct Laser Ablation

In the laser ablation process, the laser beam is directed to the working material surface and causes material loss from the surface due to heating. This situation occurs when the work material melts and evaporates from the irradiated area [38]. Material removal in the laser ablation process is due to the production of nanoparticles upon heating and melting the targeted material with the irradiated laser pulse [37]. Micro geometries realized with ultra-short pulse laser ablation technique provide advantages in terms of high accuracy, repeatability and heat [39].

Dawit Zenebe Segu et al. showed that using a pulsed Nd YAG laser, textures using circles and ellipses together on the surface of AISI 52100 steel were produced by laser ablation process (Figure 4). It has been observed that the friction coefficient of the textured surface is lower and more stable than the untextured surface. The 12% density textured surface was found to be most effective in reducing friction under test conditions (Figure 4). The positive effect of multi-scale dimples on the friction coefficient increases with dimple depth and sliding speed [40].

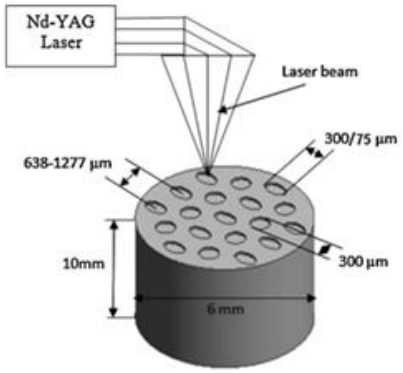


Figure 4. Schematic of laser surface texturing with laser ablation technique [40]

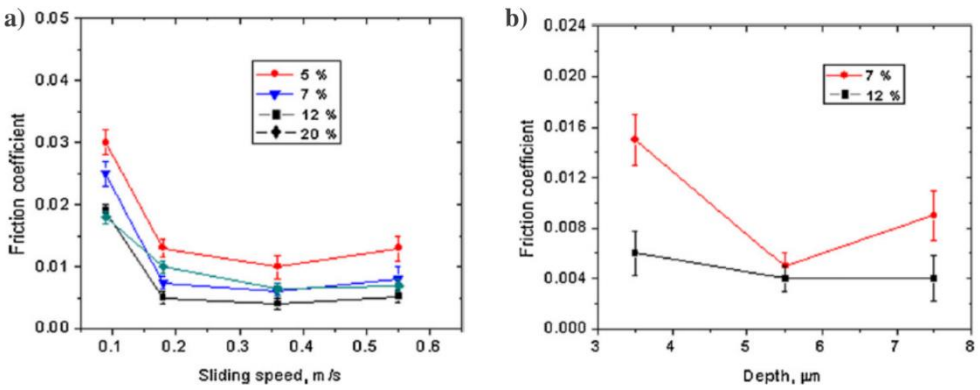


Figure 5. a) The friction coefficient of multi-scale LST with increasing sliding speed at different dimple densities b) the friction coefficient of multi-scale LST with dimple densities of 7 and 12% at different dimple depths [40]

Dawit Zenebe Segu et al. performed laser ablation by combining different shapes such as circle-square and circle-triangle on steel disc samples (Figure 6). The effect of the area density of the pits on the tribological performance was investigated under dry and coated MoS2 film [41].

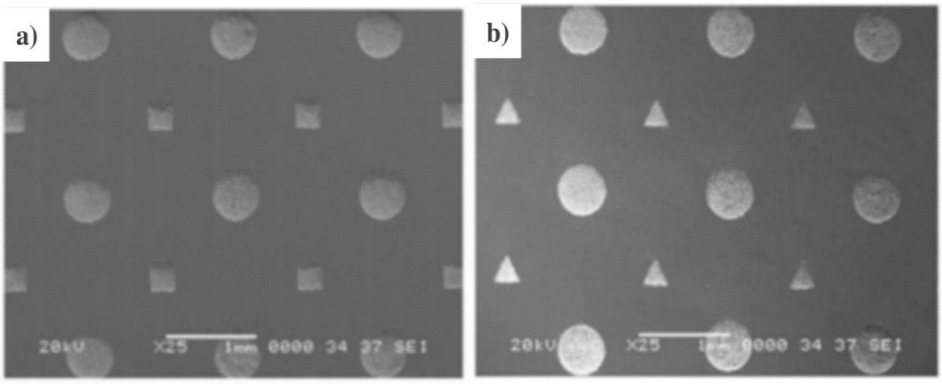


Figure 6. The surface of textured a) circle-squares b) circle-triangles [41]

### 2.2. Direct Laser Interference Patterning (DLIP)

With the laser beam, the surface material of the samples is melted locally and at the highest laser intensity. Periodic surface geometries, such as dot, line, and cross patterns, can be produced on a variety of materials. The spacing between the textures produced is determined by the laser wavelength, the laser target distance, and the distance between the two lasers [27]. Periodic patterns with feature sizes ranging from 5 micrometers to 15 micrometers can be created on the surface of many engineering materials [42]. Compared to laser ablation, laser interference provides higher texture resolution and the heat-affected zone is smaller. Despite the advantages that LST offers through direct laser ablation and laser interference, the heating effect in these approaches can lead to undesirable situations such as material deformation, phase transformation, thermal stresses [27].

### 2.3. LST by Laser Shock Processing

The target material is coated with an opaque coating to absorb the laser energy. A transparent confinement is made on the coating. During the LSP process, the laser pulse interacts with the opaque coating instead of the target material, resulting in laser-induced plasma formation. Expansion of the plasma is limited by a transparent confinement. This situation leads to the generation of a laser-induced shock wave that propagates through the target material (Figure 7). When the shock wave pressure exceeds the dynamic yield strength of the target materials, very high strain rate plastic deformation occurs on the surface of the machined specimens [27].

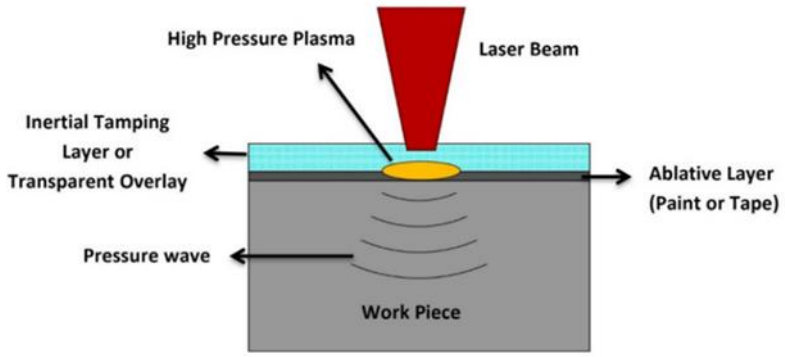


Figure 7. Schematic of laser shock processing [43]

Experiment by Wei Guo et al revealed that the samples exhibited more intensive Aluminum in layers after LSP; Therefore, it can be concluded that LSP improves the oxidation resistance of Ti6Al4V titanium alloy produced through Laser Additive Manufactured (LAM) [25].

A new processing technique called indirect laser shock surface patterning (LSSP) (Figure 8) has been found for the scalable production of texture shapes with LSP. In the indirect LSSP method, a micro mold with micro properties is placed on the surface of the material to be textured. After that, the micro mold is covered with ablative coating. This coating is applied to absorb laser energy and protect micropatterns and target sample surfaces from laser damage. A transparent confinement is placed over the ablative coating. The transparent confinement is used to limit the hydrodynamic expansion of the laser-induced plasma. This method helps the sample act as a cushion for texturing to prevent it from interacting directly with the laser energy [44].

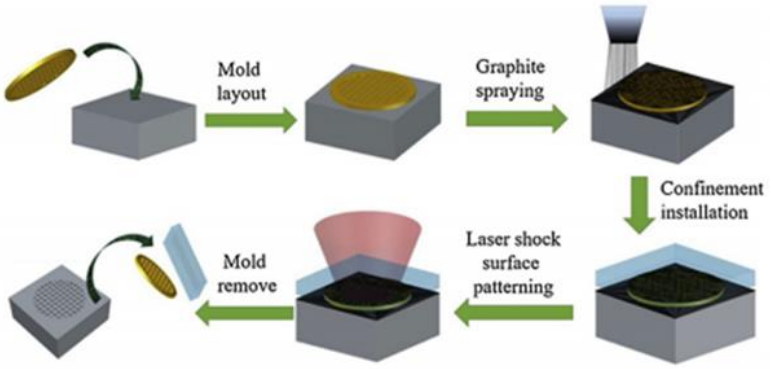


Figure 8. Schematic of indirect LSSP [44]

## 3. Effects of Laser Parameters on Surface Texturing

While performing the LST process, laser processing parameters such as the power density of the laser, the number of pulses and scanning speed can be controlled by adjusting. Understanding the effects of these parameters on the surface texture, determining the appropriate parametric levels, optimum design of LST processes will be helpful in improving the tribological performance of the processed materials. This section reviews the key parameters that affect the required surface texturing and the basic mechanisms related.

### 3.1. Laser Power Intensity

Laser power intensity (LPI) is one of the most critical LST processing parameters to determine the surface texturing effect [37]. For ablation-based and interference-based LST processes, laser power intensity affects the amount of laser energy that determines the width, depth, and shape of texture features as well as the heat-affected zone [27].

Seung Jai Won et al. applied laser surface texturing using a mesh grid mask (25 micrometer bar width) with Nd: YAG pulsed laser on an aluminum surface (Figure 9). The effects of laser intensity and laser pulse numbers were investigated by experiments. According to the experiments performed at 0.39, 3.9 and 7.8 GW/cm2 laser intensities, the surface roughness (Ra) values were found to be 1.7, 2.1 and 3.0 micrometers, respectively (Figure 10a). As a result of these, with the increase of laser intensity up to 3.9 GW/cm2, an increase in surface roughness was observed as the mass under the hole melted more and then solidified. If the laser intensity was 7.8 GW/cm2, the area where the mesh grid part contacts to the sample melted and welded to that part due to high laser intensity (Figure

10b). This situation has caused the surface of the hole region to become more irregular than the others, and thus the surface roughness has increased considerably [45].

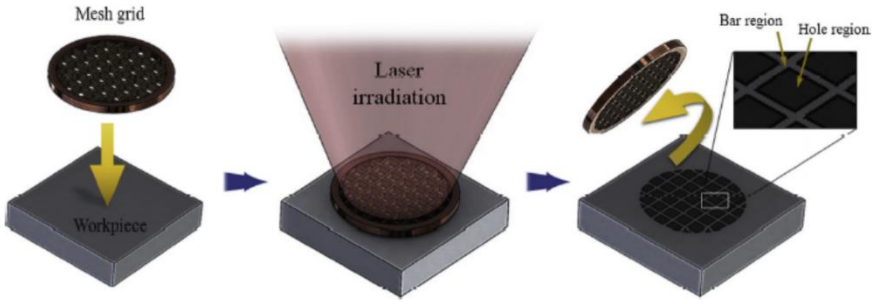


Figure 9. Schematic of experimental procedure [45]

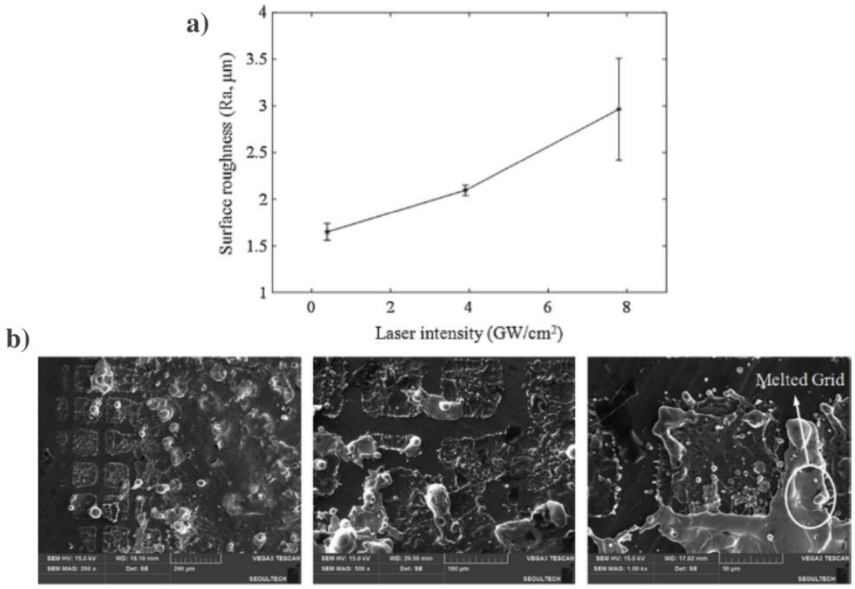


Figure 10. Surface morphologies after masked laser surface texturing with 7.8 GW/cm2 laser intensity a) surface roughness values (Ra) of the laser textured specimens at different laser intensities b) SEM images with different magnifications [45]

### 3.2. Number of Laser Pulses

In the LST process, the number of pulses is an important parameter for the geometry of the texture features.

Seung Jai Won et al., in their experiment, according to the results obtained under 1, 5, 10 and 20 laser pulse numbers on the aluminum, it was observed that the average depth of the bar increased at 5 and 10 pulses by 75% and 170%, respectively. On the other hand, the roughness of the hole decreased in both experiments. In the number of 20 laser pulses, a 70% increase in the width of the bars (Figure 11a) was observed, and in this case micro-scale holes were formed due to the accumulated thermal effect. Compared to the number of single laser pulses, the surface roughness values of the hole region at different laser pulse numbers decreased at 5 and 10 laser pulses by 48.7% and 77%, respectively. No change was observed in the surface roughness at 20 pulses (Figure 11b) [45].

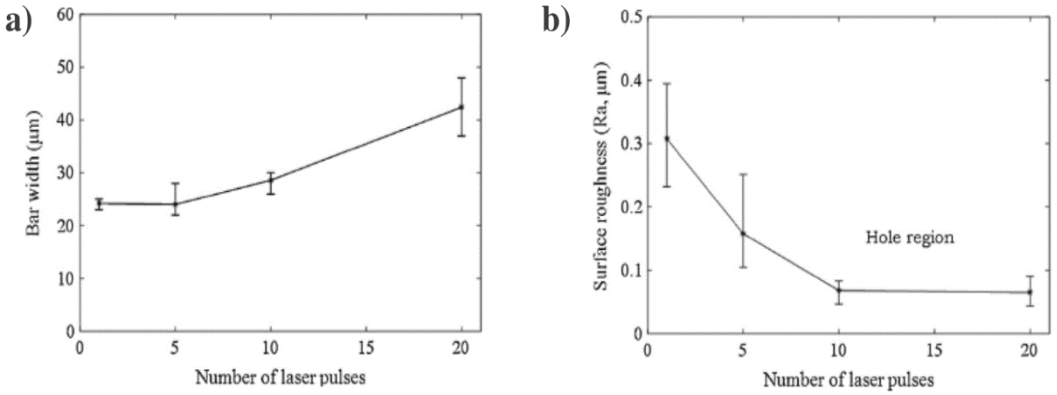


Figure 11. a) Bar width, b) surface roughness (Ra) of hole region as a function of number of laser pulses (0.39 GW/cm2 laser intensity) [45]

### 3.3. Laser Scanning Speed

Scanning speed is one of the important laser parameters that significantly affect the surface roughness, texture depth, surface processing efficiency and microstructure of engineering materials.

In the experiment on Ti6Al4V of Xiaoying Xi et al., the scanning speed was changed from 10mm/s to 40mm/s in the case where the average power was 14.3W and the repetition rate was 30kHz. It was observed that with the increase of scanning speed, the depth decreased (Figure 12). At 40 mm/s, the amount of melt was the maximum and the depth was the smallest. The scanning speed, in which the surface quality was better than the others, was found to be in the range of 10-20 mm/s [46].

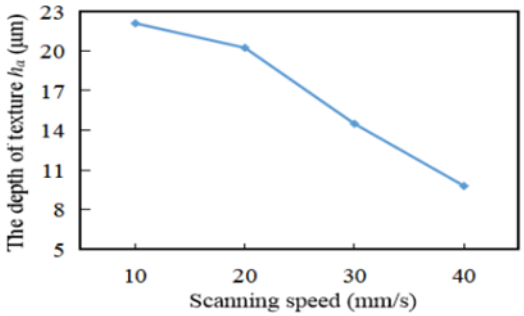


Figure 12. The relationship between $h_a$ and scanning speed [46]

## 4. Enhanced Tribological Performance of Engineering Materials by LST

Tribological examination of laser parameters in the creation of textured surface textures is necessary to improve their tribological properties. The textured surface textures were studied in dry or lubricated conditions for coefficient of friction and wear resistance. It is important to understand the impact of the above parameters for the design of LST applied engineering materials and the correct selection of suitable parameters.

### 4.1. Texture Design

Certain types of textures are created on samples treated with LST. One of the texture types is shown in Figure 13 as an example. It is important to establish the contact between texture parameters

and tribological properties for better design of the LST process. In this section, the effects of the tribological properties of texture density, size and depth, and texture shape on engineering materials are investigated.

Figure 13. LST regular micro-surface structure in the form of micro-dimples [28]

### 4.1.1. Texture Density

Texture density is one of the important laser parameters that affect the tribological behavior of LST processed engineering materials. The effects of texture density on wear rate and coefficient of friction were examined from the literatures.

Shuaishuai Zeng et al. performed tests on 1-Dimple and 3-Dimple samples produced on the stator surface of PTFE-based material. As a result of the test lasting 100 hours, the transfer material on the stator surface decreases as the dimples increase. It caused a reduction in the adhesion wear of the friction material due to texturing. Compared to the non-textured stator, the wear rate of the sliding friction material against the 3-dimple stator was 51.9% reduced (Figure 14) [47].

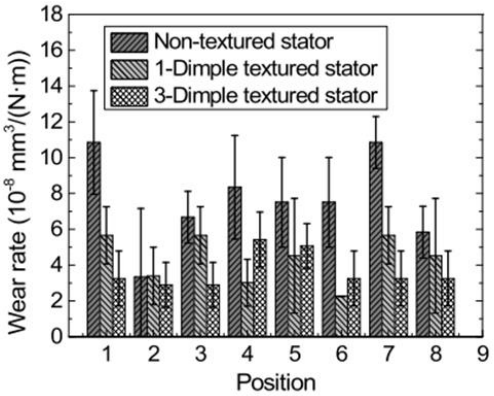


Figure 14. Wear rate of friction material [47]

According to the review by Vijay Kumar et al., the friction coefficient on the steel substrate decreased from 0.42 to 0.24 in the pin wear test (Figure 15) performed on the disc at 50% textured density [37].

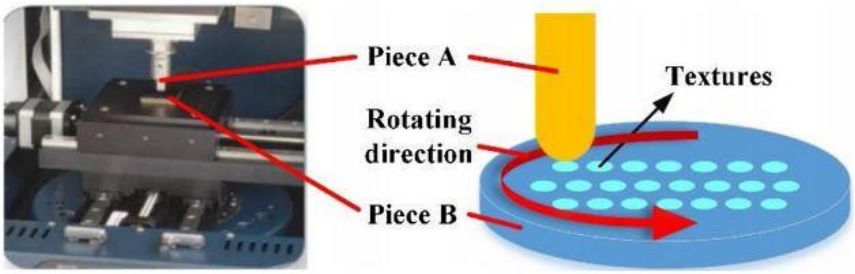


Figure 15. Schematic diagram of unidirectional rotating frictions tests [37]

Andriy Kovalchenko et al. used dimpled flat parts in their tribological experiments using oils of different viscosities (Figure 16) in a pin-on-disk friction machine. It was observed that abrasive wear increased in 5100 steel ball of discs with higher dimple density [49].

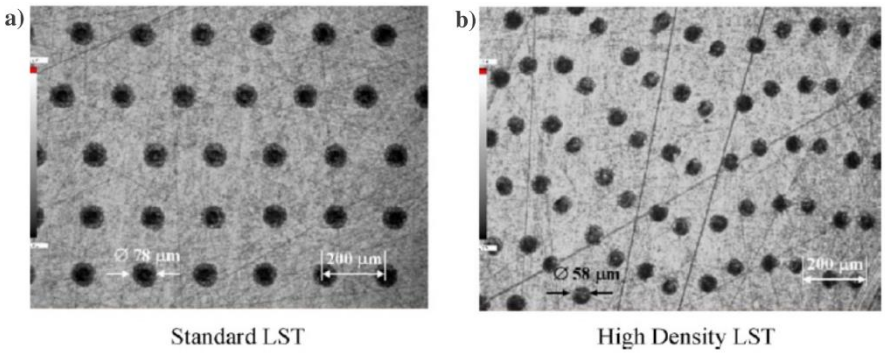


Figure 16. Optical micrographs of various disc surfaces used for testing [49]

### 4.1.2. Size and Depth

Another parameter affecting the tribological performance of engineering materials is texture size and depth. In this section, the effects of texture size and depth on tribological performance are examined.

Min Ji et al. produced micro tissues by laser ablation on zirconium ceramic surfaces and examined the effects of these textures on their tribological behavior. In the experiment, measurements were made on the surface at different depths and widths. The best friction performance was seen at the greatest depth that is 11 micrometers and smallest width that is 20 micrometers. (Figure 17). A small groove width is beneficial for tribological performance. With an appropriate increase in depth, tribological behavior can be greatly improved [29].

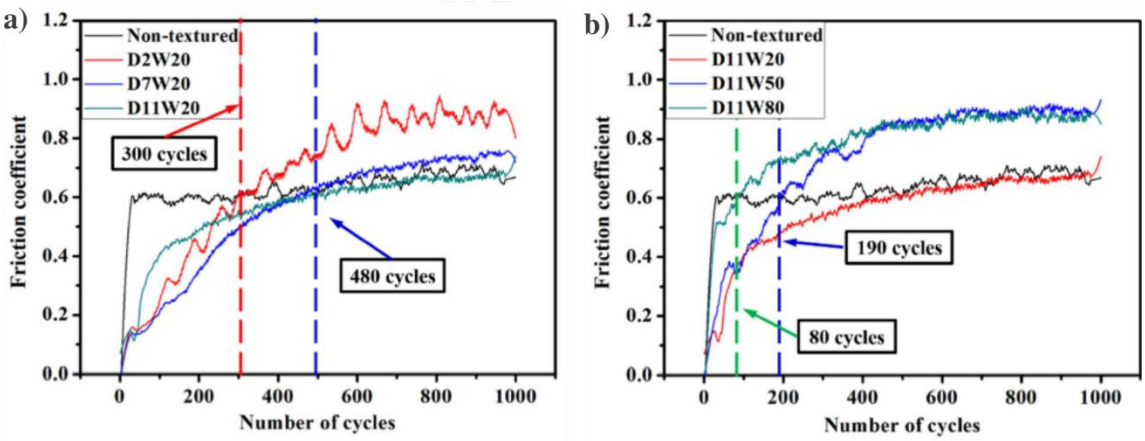


Figure 17. The curves of the friction coefficients versus different surface textures: a) different groove depths and b) different groove widths [29]

### 4.1.3. Texture Shape

There are various patterns in LST techniques. In this section, studies on tribological parameters about various patterns from different literatures are examined.

Demofilo ´ Maldonado-Cort´es et al. have mentioned that there are two different types of textured geometry, discrete (closed) geometries and continuous (open) geometries (Figure 18). Geometry such as circle, triangle, rectangle, and square are examples of discrete geometries. Patterns such as circle, triangle, rectangle, and square are examples of discrete geometries. Patterns such as micro-grooves, crosshatch are examples of continuous geometries. COF and wear values were examined under three different pressures on the AISI D2 steel by applying a PAO4 lubricating fluid under reciprocating test conditions. According to the experiment, the best results were observed with 38% COF reduction and 57% wear value reduction on the circle textured surface at low pressure. At high pressures, 78% COF reduction and 54% wear value reduction were observed on the S-shaped textured surface [50].

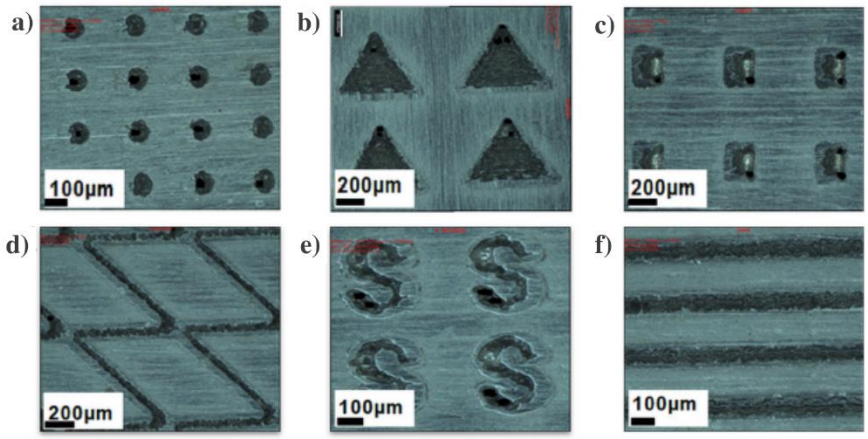


Figure 18. SEM images of LST geometries (2D), from top left to bottom right: a) circles, b) triangles, c) squares, d) crosshatch, e) “S” shape and f) lines [50]

Karthikeyan et al. performed circle, ellipse, hatch and grid pattern texturing on samples made of Ti6Al4V titanium alloy and examined the friction coefficients on the samples. Among these patterns,

the maximum friction coefficient in the grid pattern and the minimum friction coefficient in the hatch pattern were observed (Figure 19) [51].

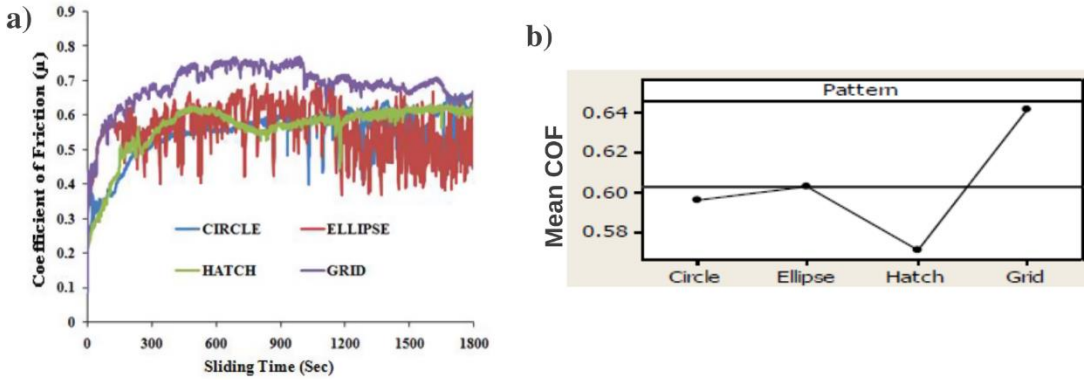


Figure 19. a) Coefficient of friction vs sliding distance for the different dimple shapes, b) the effects of pattern shape on COF [51]

### 4.2. Coefficient of Friction and Wear Resistance by LST

The determination of the coefficient of friction in engineering materials is important for the tribological performance of the system. The coefficient of friction and wear resistance vary in dry or lubricating conditions, in different shapes and densities. The effects of starved lubrication on the friction coefficient and wear resistance along with different parameters are discussed.

#### 4.2.1. Dry

The effect of LST textures produced in engineering materials on COF and wear rate was investigated under dry conditions. It has been observed that laser surface texturing prevents wear debris in circular, square and triangular patterns in dry sliding conditions [52].

Tianchang Hu et al. produced micro dimple densities (13%, 23%, 44%) on the Ti-6Al-4V surface. The effects of these densities on the friction behavior in the material were investigated with dry friction and $MoS_2$ solid lubricant film coating. In the experiments performed under 1 N load in dry friction, it was observed that the wear increased at lower dimple density. On the other hand, it was concluded when the dimple density increased, the wear and the coefficient of friction decreased. When the load was increased to 7 N, it was observed that wear particles and wear tracks accumulated on the untextured surface and the low-density surface, and the surface exhibited a severely deformed plastic state. With 44% dimple density, the surface had a lower coefficient of friction and a longer wear life (Figure 20) [53].

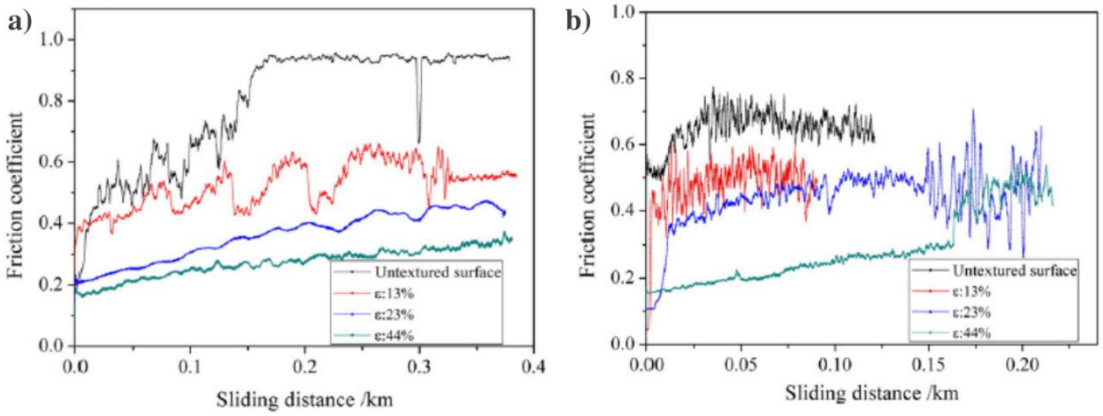


Figure 20. Friction coefficients variation as a function of sliding distance for the untextured and textured surfaces under dry friction: (a)1 N, 5 cm/s; (b) 7 N, 5 cm/s. ε indicates the dimples density [53]

### 4.2.2. Lubricated

The effect of LST textures produced in engineering materials on COF and wear rate was investigated under lubricated conditions. Different solid lubricants in the tested materials vary in the coefficient of friction [54].

Yixu Niu et al. produced dimples with different areal densities, diameters and depths on the surface of medium carbon steel. In case of starved lubrication on the samples, tests were carried out for friction and wear properties. For each test, 0.1 microliter of PAO4 oil was added to the contact point of the ball and disc. As a result of these experiments, the best friction coefficient and wear rate were obtained on textured surfaces with a depth of 10 micrometers, an area density of 10% and a diameter of 100 micrometers (Figure 21). In the case of starved lubrication, the amount of solid-solid contact increased and the dimple structures were abraded. This wear resulted in dry friction as no additional oil could be transferred to the contact area. After this case, the friction coefficient started to increase rapidly. The increase in the friction coefficient caused too much heat accumulation in the contact area. As a result, strong adhesive wear and oxidation of the surface were observed (Figure 22) [55].

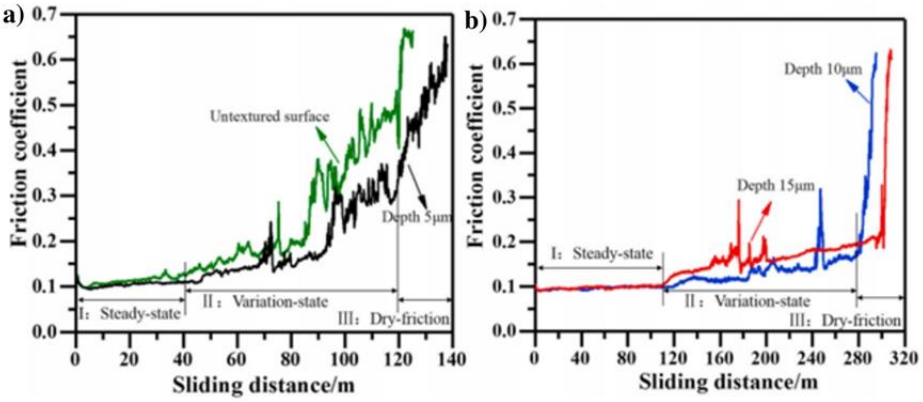


Figure 21. The friction coefficient curve of (a) untextured surface and textured surface with depth of 5 μm, and (b) depth of 10 and 15 μm [55]

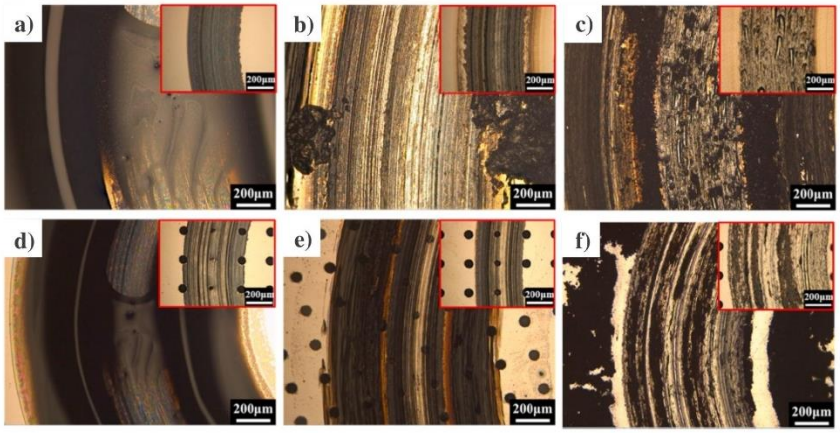


Figure 22. Optical image of the worn surface of untextured sample with sliding distance of 20 m (a), 50 m (b) and 120 m (c); and the worm surface of textured samples with depth of 5 µm where sliding distance is 30 m (d), depth of 10 µm with sliding distance of 200 m [55]

## 5. Conclusion

This review presents research to improve the tribological performance of surface texturing and methods on engineering materials. Different application areas and materials where LST improves tribological performance are mentioned. Direct laser ablation, direct laser interference patterning and direct laser shock process methods are discussed as LST generation techniques. The effects of laser power density, laser pulse numbers and scanning speeds on textured surfaces are mentioned as laser parameters. Textures on LST processed surfaces are discussed in terms of density, size, depth and shape. It provides the examination of COF and wear resistance, which are important parameters of tribological performance, under dry and lubricated conditions. It is envisaged that this review can provide guidance and information for the future design of LST processes to improve tribological performance of engineering components for various applications.

**Conflict of Interest:** This paper has been presented at the IOCENS'21 (International Online Conference on Engineering and Naturel Sciences) held in Gümüşhane (Turkey), July 5-7, 2021.

**Financial Disclosure:** The authors declared that this study has received no financial support.

## References

[1] Ryk G, Etsion I. (2006). Testing piston rings with partial laser surface texturing for friction reduction. Wear, 261, 792–796.

[2] Shang, Q., Yu, A., Wu, J., Shi, C., & Niu, W. (2017). Influence of heat affected zone on tribological properties of CuSn6 bronze laser dimple textured surface. Tribology International, 105, 158-165.

[3] Long, J., Chu, P., Li, Y., Lin, J., Cao, Z., Xu, M., . . . Xie, X. (2022). Dual-scale porous/grooved microstructures prepared by nanosecond laser surface texturing for high-performance vapor chambers. Journal of Manufacturing Processes, 73, 914-923.

[4] Huang, W., Ordikhani-Seyedlar, R., Samanta, A., Shaw, S., & Ding, H. (2022). Quantification of superhydrophobic functionalization for laser textured metal surfaces. Colloids and Surfaces A: Physicochemical and Engineering Aspects, 636, 128126.

[5] Marchetto D, Rota A, Calabri L, Gazzadi G, Menozzi C, Valeri S. (2008). AFM investigation of tribological properties of nano-patterned silicon surface. Wear, 265, 577–582.

[6] He, X., Cai, C., Zhao, H., Wang, G., Lv, L., Yan, D., & Ma, P. (2021). Effect of ion beam etching on surface/subsurface structural defect evolution in fused silica optics. Optical Materials, 116, 111096. doi:https://doi.org/10.1016/j.optmat.2021.111096

[7] Okabe, T., Yano, T., Yatagawa, K., & Taniguchi, J. (2021). Polyimide moth-eye nanostructures formed by oxygen ion beam etching for anti-reflection layers. Microelectronic Engineering, 242-243, 111559.

[8] Pettersson U, Jacobson S. (2004). Friction and wear properties of micro textured DLC

coated surfaces in boundary lubricated sliding, Tribol Lett, 17, 553–559.

[9] Bute, M., Dhole, S. D., Bhoraskar, V. N., Abhyankar, A., Terashima, C., Gosavi, S. W., & Fujishima, A. (2021). Benzophenone doped polydimethylsiloxane: Resist platform for MeV electron beam lithography assisted microlens array fabrication. Microelectronic Engineering, 250, 111632.

[10] Sugihara, T., Nagai, S., & Kaneko, A. (2022). High-aspect nano-groove fabrication in thick film resists using 150-kV high acceleration voltage electron beam lithography. Precision Engineering, 74, 205-208.

[11] Sheu, C.-R., Wang, T.-J., & Lin, C.-H. (2021). Homeotropic liquid crystal alignments through periodically unidirectional nano-wedges patterned by nanoimprint lithography. Micro and Nano Engineering, 12, 100090.

[12] Li, N., Xu, E., Liu, Z., Wang, X., & Liu, L. (2016). Tuning apparent friction coefficient by controlled patterning bulk metallic glasses surfaces. Scientific Reports, 6(1), 39388.

[13] Boinski, A.-K., Riemer, O., Karpuschewski, B., Schneider, M., Guttmann, M., & Worgull, M. (2022). Fast tool machining and hot embossing for the manufacture of diffractive structured surfaces. Precision Engineering, 74, 12-19.

[14] Liu, X., Li, K., Shen, J., & Gong, F. (2021). Hot embossing of moth eye-like nanostructure array on transparent glass with enhanced antireflection for solar cells. Ceramics International, 47(13), 18367-18375.

[15] Chen, L., Liu, Z., & Shen, Q. (2018). Enhancing tribological performance by anodizing micro-textured surfaces with nano-MoS2 coatings prepared on aluminum-silicon alloys. Tribology International, 122, 84-95.

[16] Sun, Y., Jin, L., Gong, Y., Wen, X., Yin, G., Wen, Q., & Tang, B. (2022). Experimental evaluation of surface generation and force time-varying characteristics of curvilinear grooved micro end mills fabricated by EDM. Journal of Manufacturing Processes, 73, 799-814.

[17] Gao, X., Cheng, X., Ling, S., Zheng, G., Li, Y., & Liu, H. (2022). Research on optimization of micro-milling process for curved thin wall structure. Precision Engineering, 73, 296-312.

[18] Ji, H., Gupta, M. K., Song, Q., Cai, W., Zheng, T., Zhao, Y., . . . Pimenov, D. Y. (2021). Microstructure and machinability evaluation in micro milling of selective laser melted Inconel 718 alloy. Journal of Materials Research and Technology, 14, 348-362.

[19] Walker, J. C., Kamps, T. J., Lam, J. W., Mitchell-Smith, J., & Clare, A. T. (2017). Tribological behaviour of an electrochemical jet machined textured Al-Si automotive cylinder liner material. Wear, 376-377, 1611-1621.

[20] Cebi, A., Demirtas, H., Aslan, M. T., Yilmaz, O., Kanber, B., & Kaleli, A. R. (2021). A novel machine tool concept: Robotic electrochemical machining. Procedia Manufacturing, 54, 203-208.

[21] Greco, A., Raphaelson, S., Ehmann, K., Wang, Q. J., & Lin, C. (2009). Surface Texturing of Tribological Interfaces Using the Vibromechanical Texturing Method. Journal of Manufacturing Science and Engineering, 131(6).

[22] Diogenes, L. (2012). Laser surface texturing-their applications. SAE International, 2012.

[23] Shivakoti, I., Kibria, G., Cep, R., Pradhan, B. B., & Sharma, A. (2021). Laser Surface Texturing for Biomedical Applications: A Review. Coatings, 11(2).

[24] Jähnig, T., & Lasagni, A. F. (2020). Laser interference patterned ta-C-coated dry forming tools. Industrial Lubrication and Tribology, 72(8), 1001-1005.

[25] Guo, W., Wang, H., Peng, P., Song, B., Zhang, H., Shao, T., . . . Yan, J. (2020). Effect of laser shock processing on oxidation resistance of laser additive manufactured Ti6Al4V titanium alloy. Corrosion Science, 170.

[26] Andrés L., Dimitri B., Tim K., Matthias B., Sebastian E., Teja R., Denise L., Jana B. (2015). Bringing the Direct Laser Interference Patterning Method to Industry: a One Tool-Complete Solution for Surface Functionalization. Journal of Laser Micro/Nanoengineering, 10(3), 340-344.

[27] Mao, B., Siddaiah, A., Liao, Y., & Menezes, P. L. (2020). Laser surface texturing and related techniques for enhancing tribological performance of engineering materials: A review. Journal of Manufacturing Processes, 53, 153-173.

[28] Etsion, I. (2004). Improving tribological performance of mechanical components by laser surface texturing. Tribology Letters, Vol. 17, No. 4, November 2004.

[29] Ji, M., Xu, J., Chen, M., & El Mansori, M. (2020). Enhanced hydrophilicity and tribological behavior of dental zirconia ceramics based on picosecond laser surface texturing. Ceramics International, 46(6), 7161-7169.

[30] Guarnaccio, A., Belviso, C., Montano, P., Toschi, F., Orlando, S., Ciaccio, G., . . . Lambertini, V. G. (2021). Femtosecond laser surface texturing of polypropylene copolymer for automotive paint applications. Surface and Coatings Technology, 406.

[31] Ryk, G., Kligerman, Y., & Etsion, I. (2002). Experimental Investigation of Laser Surface Texturing for Reciprocating Automotive Components. Tribology Transactions, 45(4), 444-449.

[32] Etsion, I. (2004). State of the Art in Laser Surface Texturing. Proceedings of ESDA04 7th Biennial Conference on Engineering Systems Design and Analysis.

[33] Riveiro, A., Abalde, T., Pou, P., Soto, R., del Val, J., Comesaña, R., . . . Pou, J. (2020). Influence of laser texturing on the wettability of PTFE. Applied Surface Science, 515.

[34] Liu, C., Aengenheister, S., Herzog, S., Deng, Y., Kaletsch, A., Schmitz, K., & Broeckmann, C. (2021). Application of Weibull theory to laser surface textured Al2O3. Journal of the European Ceramic Society, 41(2), 1415-1426.

[35] Tan, C., Su, J., Feng, Z., Liu, Y., Chen, B., & Song, X. (2021). Laser joining of CFRTP to titanium alloy via laser surface texturing. Chinese Journal of Aeronautics, 34(5), 103-114.

[36] Valeri, S., Gualtieri, E., & Borghi, A. (2013). Laser Surface Alloying. Encyclopedia of Tribology, 1938–1947.

[37] Vazquez-Martinez, J. M., Salguero, J., Blanco, E., & González-Leal, J. M. (2019). Nanosecond Pulsed Laser Irradiation of Titanium Alloy Substrate: Effects of Periodic Patterned Topography on the Optical Properties of Colorizing Surfaces. 9(10), 658.

[38] Vencl, A., Ivanovic, L., Stojanović, B., Zadorozhnaya, E., Mıladınović, S., & Svoboda, P. (2019). Surface texturing for tribological applications: a review. Serbıatrıb‘19 16th international conference on tribology.

[39] Mezzapesa, F. P., Scaraggi, M., Carbone, G., Sorgente, D., Ancona, A., & Lugarà, P. M. (2013). Varying the Geometry of Laser Surface Microtexturing to Enhance the Frictional Behavior

of Lubricated Steel Surfaces. Physics Procedia, 41, 677-682.

[40] Segu, D. Z., Choi, S. G., Choi, J. h., & Kim, S. S. (2013). The effect of multi-scale laser textured surface on lubrication regime. Applied Surface Science, 270, 58-63.

[41] Segu, D. Z., Kim, J.-H., Choi, S. G., Jung, Y.-S., & Kim, S.-S. (2013). Application of Taguchi techniques to study friction and wear properties of MoS2 coatings deposited on laser textured surface. Surface and Coatings Technology, 232, 504-514.

[42] Klotzbach, U., Washio, K., Kling, R., Lasagni, A. F., Gachot, C., Trinh, K. E., . . . Mücklich, F. (2017). Direct laser interference patterning, 20 years of development: from the basics to industrial applications. Paper presented at the Laser-based Micro- and Nanoprocessing XI.

[43] Gujba, A., K., & Medraj, M. (2014). Laser peening process and ıts ımpact on materials properties in comparison with shot peening and ultrasonic ımpact peening. Materials 2014.

[44] Mao, B., Siddaiah, A., Liao, Y., & Menezes, P. L. (2018). Surface texturing by ındirect laser shock surface patterning for manipulated friction coefficient. Journal of Materials Processing Technology.

[45] Won, S. J., & Kim, H. S. (2019). Effects of laser parameters on morphological change and surface properties of aluminum alloy in masked laser surface texturing. Journal of Manufacturing Processes, 48, 260-269.

[46] Xi, X., Pan, Y., Wang, P., & Fu, X. (2019). Effect of Laser Processing Parameters on Surface Texture of Ti6Al4V Alloy. IOP Conference Series: Materials Science and Engineering.

[47] Zeng, S., Li, J., Zhou, N., Zhang, J., Yu, A., & He, H. (2020). Improving the wear resistance of PTFE-based friction material used in ultrasonic motors by laser surface texturing. Tribology International, 141.

[48] Yang, L., Ding, Y., Cheng, B., He, J., Wang, G., & Wang, Y. (2018). Investigations on femtosecond laser modified micro-textured surface with anti-friction property on bearing steel GCr15. Applied Surface Science, 434, 831-842.

[49] Kovalchenko, A., Ajayi, O., Erdemir, A., & Fenske, G. (2011). Friction and wear behavior of laser textured surface under lubricated initial point contact. Wear, 271(9-10), 1719-1725.

[50] Maldonado-Cortés, D., Peña-Parás, L., Martínez, N. R., Leal, M. P., & Quintanilla Correa, D. I. (2021). Tribological characterization of different geometries generated with laser surface texturing for tooling applications. Wear.

[51] Karthikeyan, A., Krishnan, R. M., Ananth, M.P., Ponnuvel, S., & Sridharan, V. (2020). Laser parameter optimization and unidirectional sliding wear performance of surface textured Ti6Al4V alloy. IOP Conference Series: Materials Science and Engineering.

[52] Krishna Kumar, P., & Sathish Kumar, A. (2021). Investigation of frictional characteristics of laser textured aluminium 6061 and aluminium 7071 alloys under dry sliding conformal contact in pin on disc tribometer. Materials Today: Proceedings, 45, 670-676.

[53] Hu, T., Hu, L., & Ding, Q. (2012). Effective solution for the tribological problems of Ti-6Al-4V: Combination of laser surface texturing and solid lubricant film. Surface and Coatings Technology, 206(24), 5060-5066.

[54] Jeong, S.-H., Kim, S.-H., Kim, T.-H., Cho, S.-H., Gyawali, G., & Lee, S. W. (2016). Effects of solid lubricant and laser surface texturing on frictional performance of pulse electric current sintered Al 2 O 3 –ZrO 2 composites. Ceramics International, 42(6), 7830-7836.

[55] Niu, Y., Pang, X., Yue, S., Shangguan, B., & Zhang, Y. (2021). The friction and wear behavior of laser textured surfaces in non-conformal contact under starved lubrication. Wear.